1.0

1.1

1.25 1.4 1.6

28 2.5

32 2.2

36

40 2.0

1.8

MICROCOPY RESOLUTION TEST CHART

NATIONAL BUREAU OF STANDARDS-1963-A

AD-A061884

SHIVA ELECTROMAGNETIC IMPLOSION X-RAY SOURCE

May 1978

Final Report

Approved for public release; distribution unlimited.

AIR FORCE WEAPONS LABORATORY
Air Force Systems Command
Kirtland Air Force Base, NM 87117

82 02 17024

This final report was prepared by the Air Force Weapons Laboratory, Kirtland AFB, New Mexico, under Job Order 88091709. Dr. William L. Baker was the Laboratory Project Officer-in-Charge.

When US Government drawingings, specifications, or other data are used for any purpose other than a definitely related Government procurement operation, the Government thereby incurs no responsibility or any obligation whatsoever, and the fact that the Government may have formulated, furnished, or in any way supplied the said drawings, specifications, or other data is not to be regarded by implication or otherwise as in any manner licensing the holder or any other person or corporation or conveying any rights or permission to manufacture, use, or sell any patented invention that may in any way be related thereto.

This report has been reviewed by the Office of Information (OI) and is releasable to the National Technical Information Service (NTIS). At NTIS, it will be available to the general public, including foreign nations.

This technical report has been reviewed and is approved for publication.

William L. Baker

WILLIAM L. BAKER, PhD
Project Officer

FOR THE COMMANDER

Norman F. Roderick

NORMAN F. RODERICK
Major, USAF
Advanced Concepts Branch

John S. DeWitt

JOHN S. DEWITT
Lt Colonel, USAF
Applied Physics Division

REPORT DOCUMENTATION PAGE	READ INSTRUCTIONS BEFORE COMPLETING FORM

1. REPORT NUMBER AFWL-TR-77-252	2. GOVT ACCESSION NO.	3. RECIPIENT'S CATALOG NUMBER

4. TITLE (and Subtitle) SHIVA ELECTROMAGNETIC IMPLOSION X-RAY SOURCE	5. TYPE OF REPORT & PERIOD COVERED Final Report
	6. PERFORMING ORG. REPORT NUMBER

7. AUTHOR(s) J. H. Degnan, W. L. Baker, M. C. Clark, J. F. Kiuttu, C. R. McClenahan, R. E. Reinosvky	8. CONTRACT OR GRANT NUMBER(s)

9. PERFORMING ORGANIZATION NAME AND ADDRESS Air Force Weapons Laboratory Kirtland Air Force Base, NM 87117	10. PROGRAM ELEMENT, PROJECT, TASK AREA & WORK UNIT NUMBERS JON: 88091709

11. CONTROLLING OFFICE NAME AND ADDRESS Air Force Weapons Laboratory Kirtland Air Force Base, NM 87117	12. REPORT DATE May 1978
	13. NUMBER OF PAGES 47

14. MONITORING AGENCY NAME & ADDRESS(if different from Controlling Office)	15. SECURITY CLASS. (of this report) UNCLASSIFIED
	15a. DECLASSIFICATION/ DOWNGRADING SCHEDULE

16. DISTRIBUTION STATEMENT (of this Report)

Approved for public release; distribution unlimited.

17. DISTRIBUTION STATEMENT (of the abstract entered in Block 20, if different from Report)

18. SUPPLEMENTARY NOTES

19. KEY WORDS (Continue on reverse side if necessary and identify by block number)

Electromagnetic Implosion	Fast Photography
Imploding Liner	Magnetic Probes
Cylindrical Foil Liner	Radiation Diagnostics
Hollow Z-Pinch	
Magnetohydrodynamic	

20. ABSTRACT (Continue on reverse side if necessary and identify by block number) The generation of pulsed high-energy density plasmas by electromagnetic implosion of cylindrical foils (i.e., imploding liners or hollow Z-pinches) has been investigated experimentally and theoretically at the Air Force Weapons Laboratory. The experimental studies involve discharging a 1.3 μs, 1.1 megajoule capacitor bank through 7 cm radius, 2 cm tall, 3 to 30 mg cylindrical foil liners. Typical discharge parameters are 7 to 12 MA peak current and 1-1.5 μs current rise time. Current and voltage waveforms indicate strong coupling of the load

DD FORM 1473 EDITION OF 1 NOV 65 IS OBSOLETE   UNCLASSIFIED

to the capacitor bank, and analysis of the waveforms indicates good implosion of the current sheath. Optical and magnetic probe measurements are consistent with 1 to 2 cm thickness of the imploding plasma shell and with final implosion velocities $\sim$15 to 20 cm/μs. Radiation diagnostic measurements indicate ultra-soft X-ray yields $\sim$50 to 100 kJ with the FWHM of the photon pulse $\sim$80 to 100 ns. The radiation data are consistent with a quasi-black body spectrum (T $\sim$30 to 50 ev) comprising most of the energy, with additional higher temperature and optically thin spectral components. The Al^{11+} and Al^{12+} line and recombination radiation is frequently observed. Comparison of electrical, magnetic, and radiation data with one dimensional magnetohydrodynamic and two dimensional magnetohydrodynamic calculations is presented. The prospects for improving the performance with the present energy source and scaling to larger energy sources are briefly discussed.

PREFACE

CONTENTS

SECTION I

INTRODUCTION

The concept of electromagnetic implosion of cylindrical plasma shells (i.e., imploding liners or hollow Z-pinches) to obtain pulsed, high-temperature, high-density plasmas has been discussed by Turchi and Baker (ref. 1). This concept has been investigated experimentally and theoretically for the past several years in the SHIVA X-ray source development program at the Air Force Weapons Laboratory. The SHIVA imploding liner concept is distinct from other imploding liner efforts (refs. 2, 3, 4) in that the idea is to produce a hot, dense plasma from the self-collapsed plasma liner itself, rather than to compress a magnetic field preformed plasma mixture.

The motivation for developing the electromagnetic implosion technique is to produce an intense pulsed X-ray source for laboratory studies of X-ray matter interaction. The X-ray emission powers of $\sim10^{13}$ watts are believed possible with existing pulsed power facilities, and powers $\sim10^{12}$ watts have already been achieved (ref. 5), as will be discussed in this paper.

A schematic representation of the basic SHIVA electromagnetic implosion concept is shown in figure 1. The basic geometry is that of a plasma Z-pinch. The load consists of a large radius, thin foil cylinder which is placed in a vacuum. A fast, high-energy capacitor bank is used to drive a very high current axially through the cylindrical load. Early in the current pulse, the joule heating vaporizes the foil and transforms it into a few ev temperature plasma. The JxB force which results from the interaction of the current with its self-magnetic field accelerates the foil-plasma to a high implosion velocity. During this acceleration phase, electrical energy from the capacitor bank is converted into kinetic energy of the imploding plasma. By proper matching of the load and electrical source, this process can occur with good efficiency (20 to 40 percent). When the plasma sheath collides with itself at the center of the implosion, its kinetic energy is rapidly converted to thermal energy, creating a hot, dense plasma which radiates much of its energy in a short burst of X rays.

To create a high-temperature, high-density plasma, large amounts of energy must be efficiently coupled to the plasma. It is considerably easier to deliver energy to kinetic energy of a moving plasma than it is to directly joule heat a
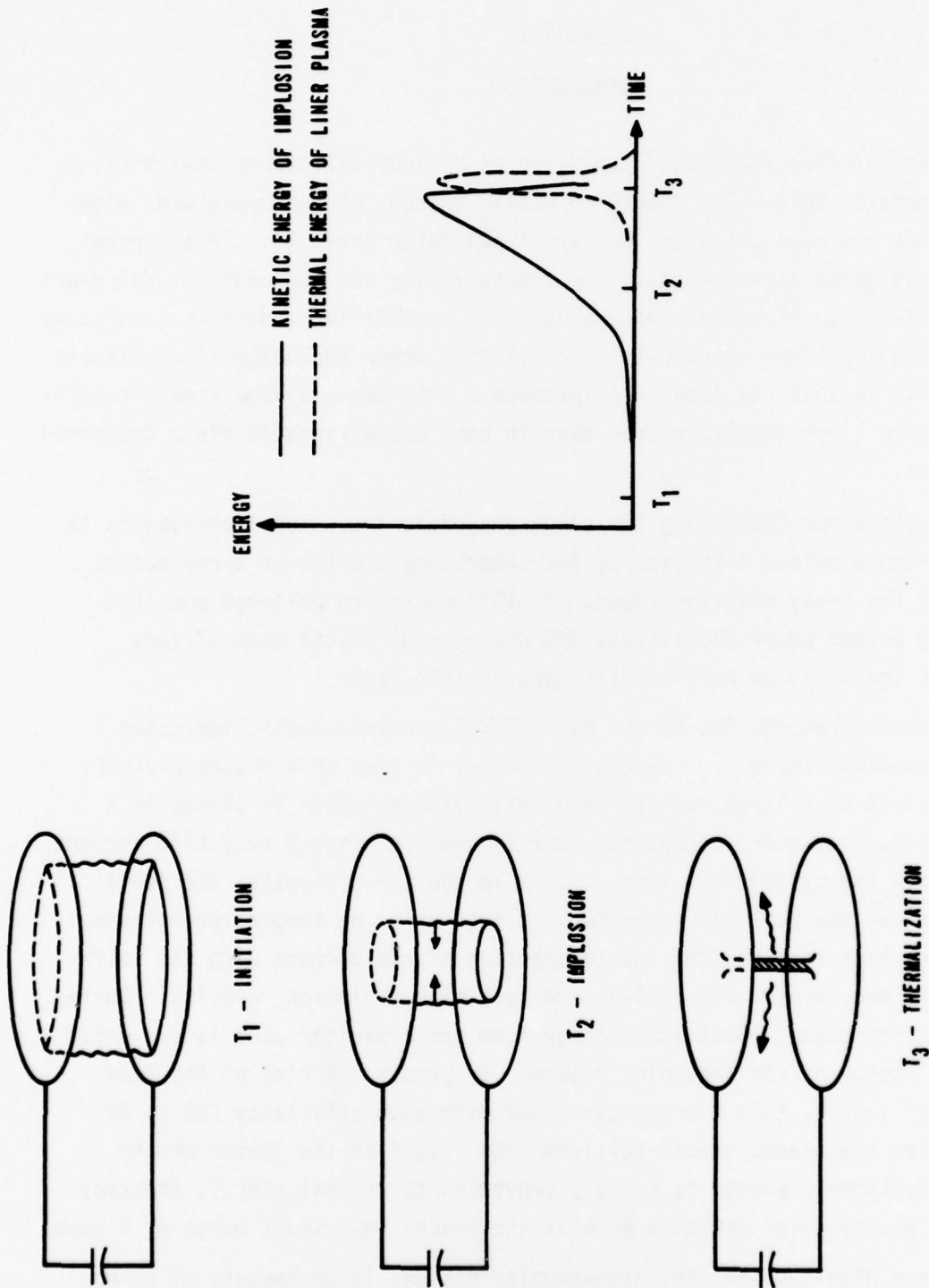
Figure 1. Electromagnetic Implosion Concept. A capacitor bank discharge through a cylindrical foil liner ionizes and implodes the liner. Upon collapse at the center, the kinetic energy of implosion is rapidly converted into plasma thermal energy.

plasma. This is because the resistance of the plasma drops as the temperature rises, making it increasingly more difficult to couple in energy. A moving plasma shell, however, has a substantial dissipative impedance regardless of temperature because its inductance is increasing with time. For an imploding foil-plasma discharge, carrying axial current J, the rate of change of inductance is

$$\frac{dL}{dt} = \frac{\mu_o h}{2\pi} \frac{u(t)}{r(t)} \tag{1}$$

where h is the height of the cylindrical discharge, μ_o is the magnetic permeability ($4\pi \times 10^{-7}$ H/m), r(t) its radius, and u(t) the implosion speed. This $\dot{L}$, which is proportional to velocity u(t), acts like a resistance with the energy dissipated by its going into kinetic energy. Since $\dot{L}$ is much greater than the plasma resistance most of the energy goes into kinetic energy and very little into internal energy during the implosion phase. Thus, with a low sheath temperature, only a small amount of energy is lost as radiation during the implosion phase.

Since the implosion load draws energy from the electrical source and stores it as kinetic energy during the implosion phase and then converts it to thermal energy at the center of the implosion, it is possible to obtain significant increase in the heating power over the power delivered by the electrical source. For an electrical source delivering energy in a one-microsecond pulse and a thermalization phase tens of nanoseconds long, the plasma can be heated at a power tens of times higher than the output of the electrical energy source. Thus, high-temperature, high-density plasmas can be created with state-of-the-art power supply technology.

Figure 2 shows typical load current and the radius of the sheath as a function of time for a load driven by a megajoule capacitor bank. Note that the foil-plasma, because of its inertia, stays near its original position for a considerable portion of the capacitor bank discharge time. During this time it presents a very low impedance; hence, the current can rise to a high value. The plasma sheath is seen to expand initially until the rapidly rising J X B driving force becomes strong enough to overcome the internal plasma pressure. The plasma sheath is then compressed and accelerated up to a high-implosion velocity.
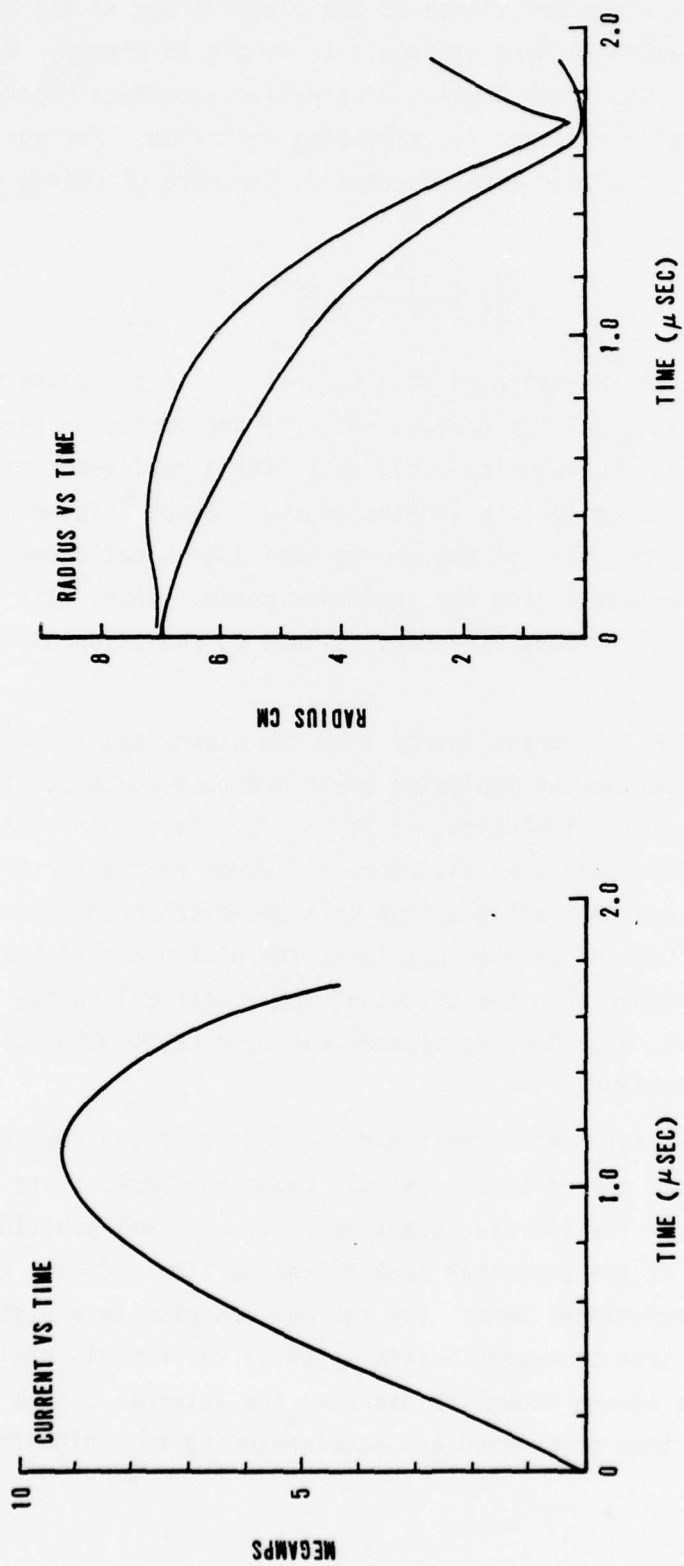
Figure 2. Current and Radius Versus Time for Imploding Liner. The Two Curves on the Radius Versus Time Plot are for the Inner and Outer Boundaries of the Plasma Liner.

To create a hot, dense plasma via the SHIVA approach, the plasma must be accelerated to a very high velocity so that a large amount of (kinetic) energy is delivered to the pinch, and that energy must be converted to thermal energy in a very short time. Velocity and sheath thickness are the most important parameters because the thermalization time is approximately equal to the thickness of the sheath divided by the velocity. For the highest temperature, the thermalization time should be minimized. i.e., the plasma should be heated at the highest possible power. This calls for minimum sheath thickness and maximum velocity consistent with good energy coupling efficiency. For a given electrical driving source, there is an optimum velocity range for high-energy transfer efficiency. If high-implosion velocities are achieved by severely cutting the sheath mass, very little kinetic energy is delivered and though the temperature may be high, the total radiation energy is low. The required higher velocities may be better obtained by using higher-powered, higher-energy electrical sources. One-dimensional magnetohydrodynamic (MHD) calculations predict a sheath thickness of a few millimeters. Experimental data show that the sheath is thicker, presumably due to plasma instabilities. Control of these instabilities, which would make the sheath more one-dimensional, is necessary for optimum load performance.

The use of a freestanding foil is critical to forming a well-behaved sheath that can run long distances during the implosion. This technique allows the discharge initiation to occur away from the insulator, unlike the classical Z-pinch in which initiation occurs across the insulator. For high-powered discharges the ultraviolet (UV) radiation is so intense it can turn the insulator surfaces into a conductor, effectively shorting out the implosion load. The use of a freestanding foil in the SHIVA geometry allows the insulator to be hidden out of sight of the UV radiation. This is especially very important for developing a technique which can be scaled up to very high energies and powers.

SECTION II

EXPERIMENT DESCRIPTION

The imploding liner studies presently underway involve discharging a 1.1 MJ capacitor bank through low-inductance imploding liner loads. The capacitor bank, illustrated in figure 3, is described in detail in reference 6. It consists of 20 capacitor bank modules spaced around a cross-shaped, low-inductance, parallel plate transmission line. At full energy the top half of each module is charged to + 50 kV and the bottom to - 50 kV. Hence, when the bank is discharged a net 100 kV is applied to the transmission line. This technique allowed the desired voltage to be obtained using available 1.85 µf capacitors. Special low-inductance, high-pressure rail gap switches were developed for the bank to minimize maintenance without compromising performance. The bank has a capacitance of 222 µf, inductance of 3 nH and stores 1.1 MJ at full voltage. The bank has been used to deliver peak currents of up to 20 MA with a current rise time of slightly over one µs. The load is located in the center of the bank.

The two liner geometries used were 10.5 cm radius, 1 cm height and 7 cm radius, 2 cm height. Both aluminum and aluminized plastic cylindrical foil liners have been used, with areal mass density of 135 to 200 µg/cm^2 for aluminum and 40 to 310 µg/cm^2 for aluminized plastic. Typical discharge parameters are 400 to 700 kJ of energy (stored at 60 to 80 kV), peak current ~7 to 12 MA current rise time ~1 to 1.5 µs and implosion velocity ~15 to 20 cm/µs.

The diagnostics included Rogowski coils, voltage probes (ref. 7), single-loop magnetic probes (ref. 8), Kerr cell shuttered and image converter fast photography, and radiation detectors. The radiation detectors included filtered metal photocathodes (X-ray diodes or XRDs) (ref. 9), silicon semiconductor (PIN) detectors (ref. 10), X-ray pinhole cameras, and convex curved crystal de Broglie spectrometers.

TO LOAD

- 50 KV +

+ 50 KV -

IMPLODING LINER CHAMBER

11 F. 100 KV. 55 KJ.
FAST CAPACITOR BANK
MODULE

~2 M

~13.6 M

TOTAL BANK:
20 MODULES
$C = 222$ μF
$L = 3 \times 10^{-9}$ H

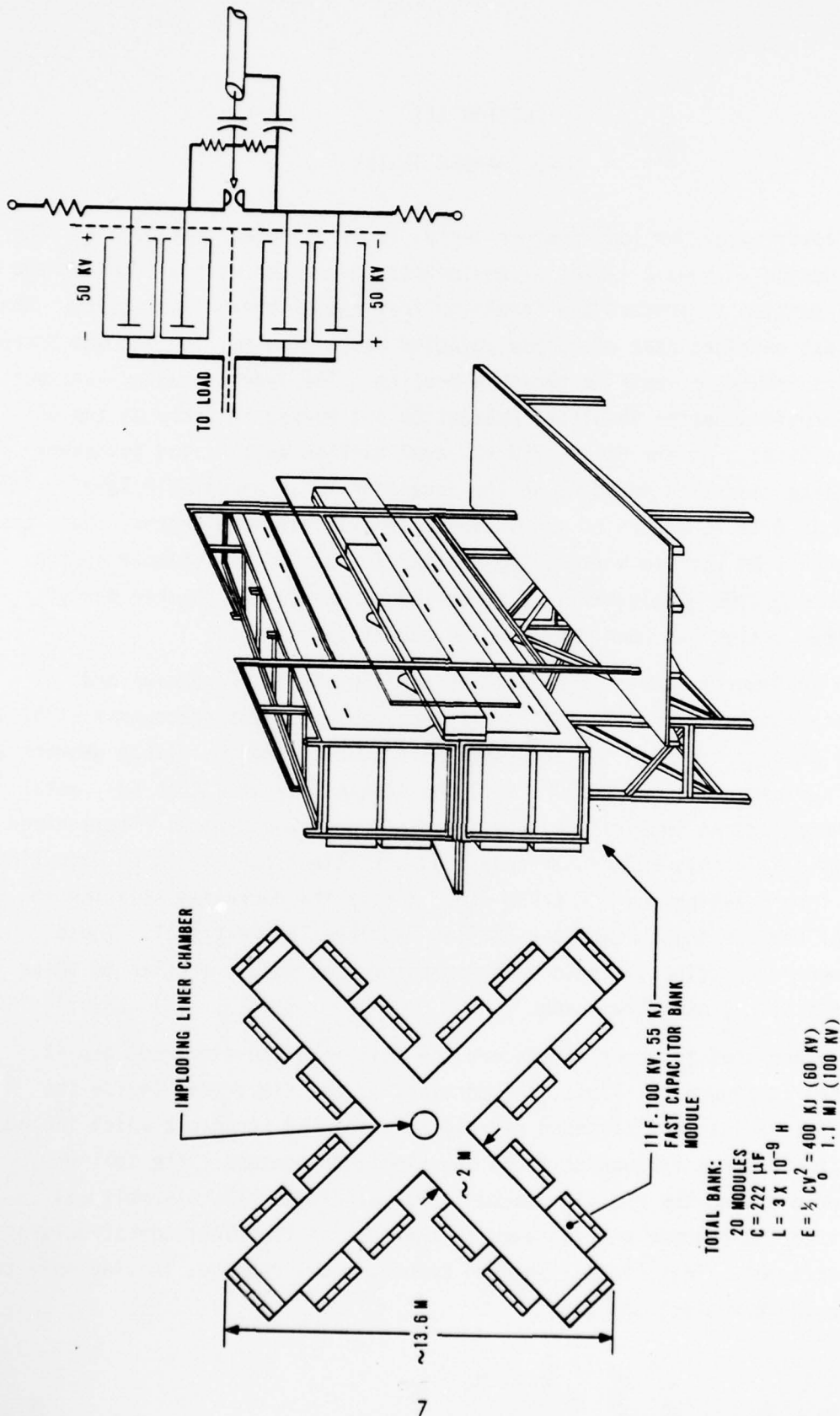$E = \frac{1}{2} C V_0^2 = 400$ KJ (60 KV)
1.1 MJ (100 KV)

Figure 3. Fast, Modular, Megajoule Capacitor Bank.

7

SECTION III

LOAD CHAMBER DESIGN

The evolution of the load chamber design is illustrated in figure 4. The earliest design -- Type A -- was a low-inductance chamber with a 1 cm gap and a coaxial section to protect the insulator from the discharge luminosity. When evidence was obtained that electrode ablation was a problem, the gap was increased to 2 cm and insulator restrike became a problem. The Type B chamber--without baffles--provided better insulator protection and worked reliably at the 60 kV, 400 kJ level. At the 80 kV, 700 kJ level baffles were needed to reduce the discharge radiation incident on the insulator to an acceptable level. This reduction is 6 to 10 orders of magnitude in the visible wavelengths. Once there was evidence that baffles worked, the coaxial feature of the chamber design was replaced by the highly-baffled, lower-inductance Type C chamber design. This chamber design has been used for all recent experiments.

Laser shadowgram studies were used to develop the baffle design and investigate insulator and electrode ablation problems. The shadowgram studies were done in a rectangular geometry simulating the cylindrical liner geometry, i.e., in a plasma rail gun (figure 5). The studies revealed that only metal baffles which are an integral part of the electrodes would work. The ionized metal baffle ablatants apparently conducted sufficient current to be magnetically confined from crossing the electrode gap. Notice the decreased ablation in regions of the gap shadowed by the baffles from the luminous foil. These studies were done using a single fast capacitor bank module similar to those used in the 1.1 MJ capacitor bank.

The method used to mount and insert the foil into the electrode gap is illustrated in figure 6. First, the portions of the electrodes inside the initial foil radius were fastened rigidly to a spacing structure which included a 2 cm diameter post through holes in the electrode centers. The foil was next wrapped around the rigidly spaced electrode disks. The assembly was lowered into the chamber and fastened to the rest of the electrode structure (as illustrated). The original spacing structure was removed, leaving only the foil bridging the electrode gap.
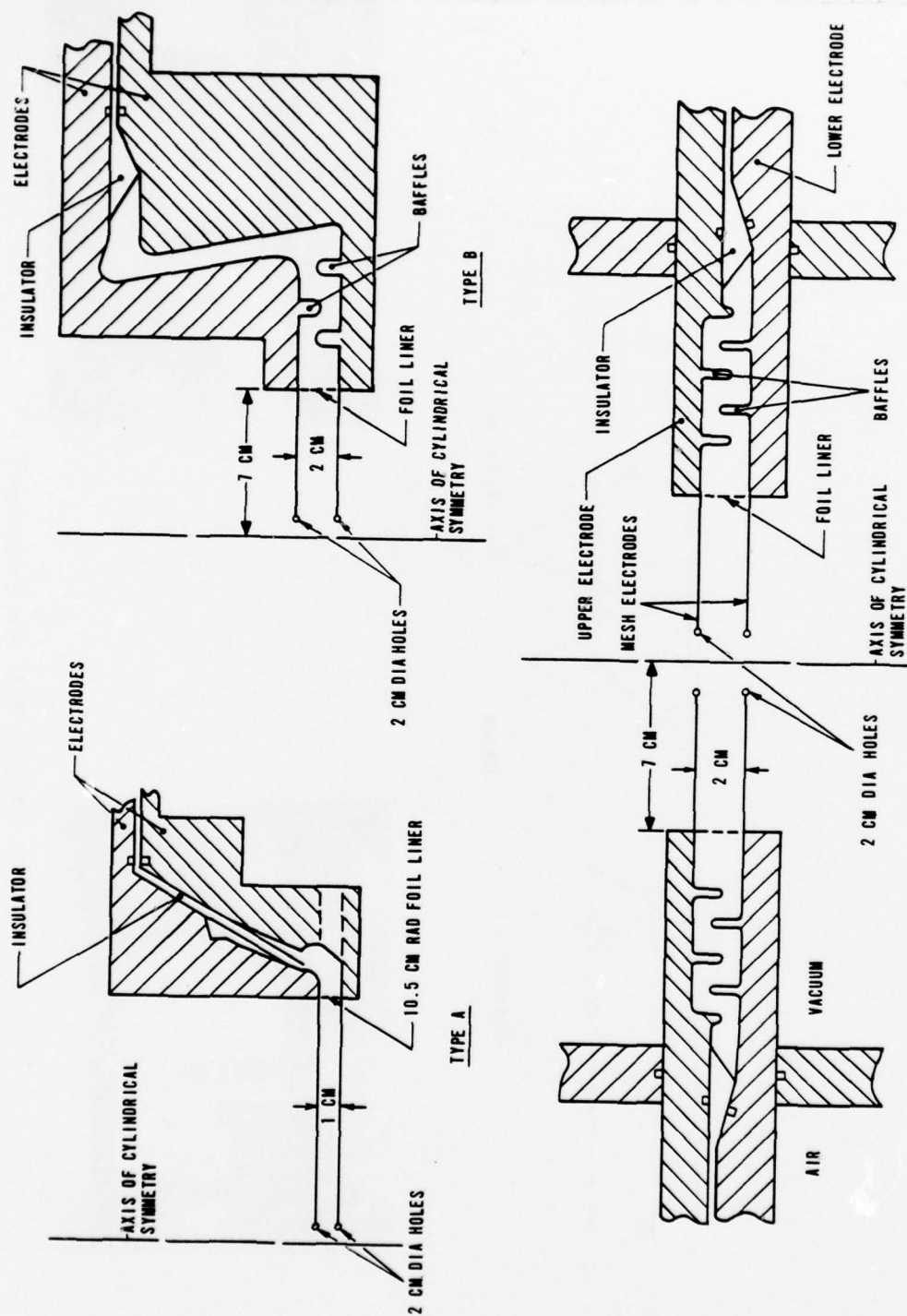
Figure 4. Shiva Implosion Chamber Electrode Geometries.
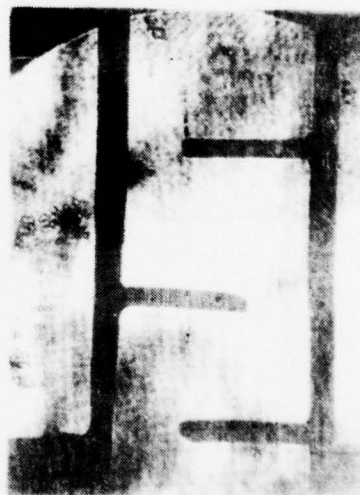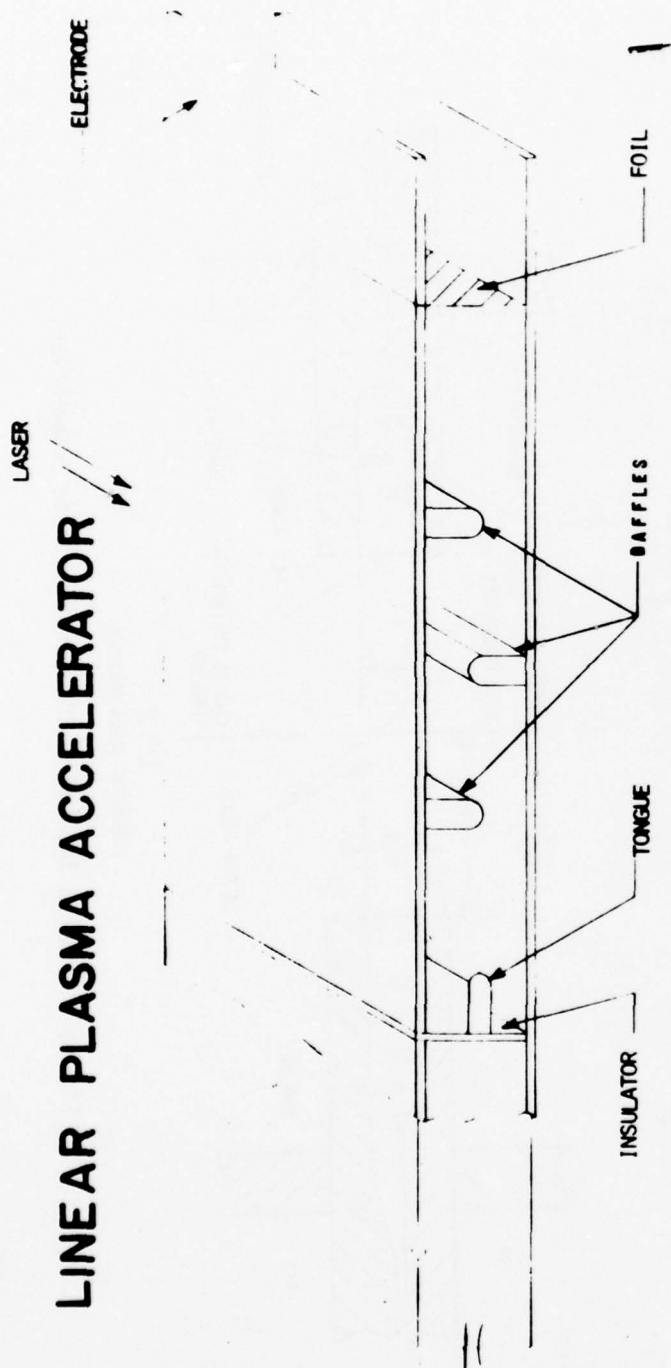
LINEAR PLASMA ACCELERATOR
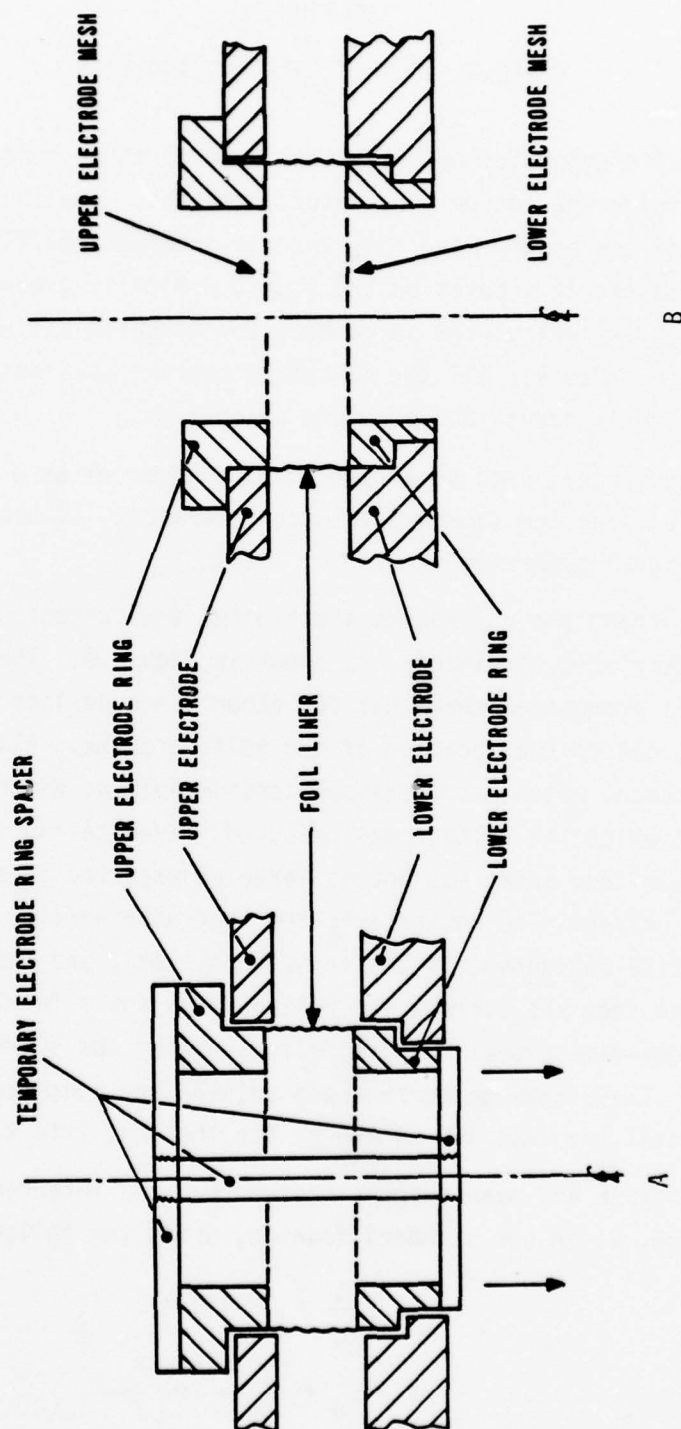

Figure 5. Plasma Rail Gun Experiment.

10

Figure 6. Foil Liner Mounting and Insertion. (A) Prior to insertion, (B) After insertion and after temporary spacer is removed.

11

SECTION IV

CURRENT, VOLTAGE DATA AND ANALYSIS

The current diagnostics normally consisted of three concentric Rogowski coils--one outside the vacuum--insulator interface, one in the baffle region (figure 4), and one between the foil and the innermost baffle. All the Rogowski loops were recessed in grooves on the lower, nominally grounded electrode (which is the anode). Typically, the calculated and measured calibrations agreed to 5 to 10 percent. Usually all the discharge current was inside the innermost Rogowski loop until about 100 ns before pinch time.

The voltage probe, used as a capacitive divider or as a $\dot{V}$ probe, was located just outside the vacuum-insulator interface. It was calibrated with a low-voltage signal generator.

Typical current and voltage data exhibited the current dips and voltage spikes characteristic of pinches, as shown in figure 7. The measured voltage spike was less pronounced than that for other pinch devices (such as dense plasma focus) due to the location of the voltage probe. All but 3.2 nH of the system inductance, which has increased considerably at pinch time, was inside the radius at which the voltage was measured. Even taking this into account, the observed voltage spike was not as large as expected in an optimum pinch. This was due primarily to restrike at the innermost baffle, about 100 ns before pinch. The time dependence of the inductance, $L(t)$, and the mean current radius $r(t)$, inferred from the current and voltage data for a fairly good implosion are compared to one-dimensional MHD predictions (using the 1D-MHD code MAGPIE, ref 11) in figure 8. The discharge current and voltage are consistent with one-dimensional prediction until the last 100 to 200 ns (or the last 1 to 2 cm) of the implosion.

The inductance and mean current radius, r, were inferred from the current, I, and voltage, V, in the standard fashion, using the following equations

$$L = \frac{1}{I} \int (V-IR)dt \tag{2}$$

$$L = L_o + \frac{\mu_o h}{2\pi} \ln \frac{r_o}{r} \tag{3}$$

where L_o is the inductance outside radius r_o. It is assumed in the data analysis that the resistive voltage is small compared to the $L\dot{I}$ and $I\dot{L}$ terms.

12

VOLTAGE & CURRENT

700 KJ

SHOT 3089
Aluminum
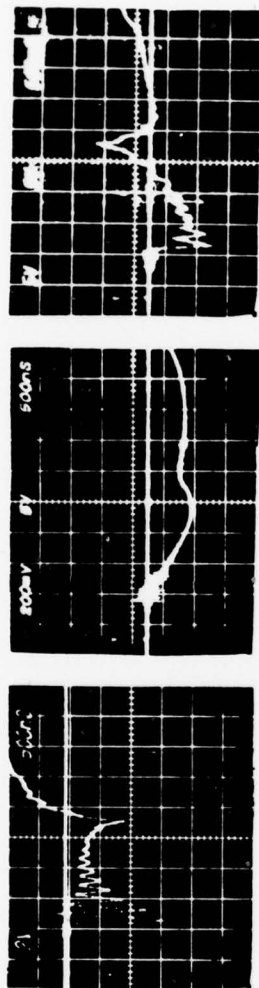
SHOT 3136
Plastic

VOLTAGE   CURRENT   DI/DT

Figure 7.   Current and Voltage Data.

Figure 8. Inductance and Radius Versus Time. Solid Lines are Obtained from Current and Voltage Data. Dotted lines are 1D-MHD predictions. The Two Dotted Line Plots for Radius Versus Time are for the Inner and Outer Boundaries of the Plasma Liner.

14

SECTION V

FAST PHOTOGRAPHY DATA

Fast visible light photographs were taken to observe the position and azimuthal structure of the luminous sheath as a function of time. Representative 50 ns exposure Kerr cell phot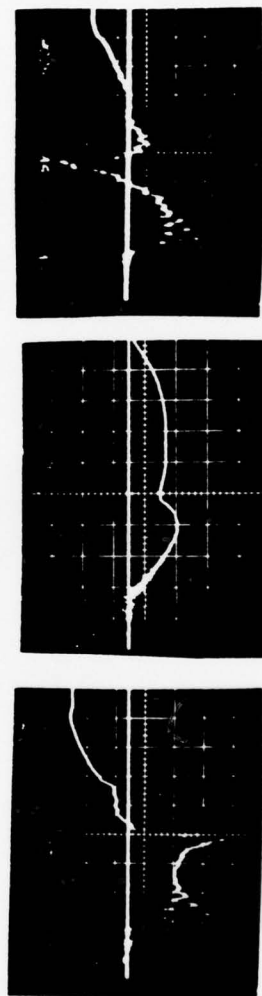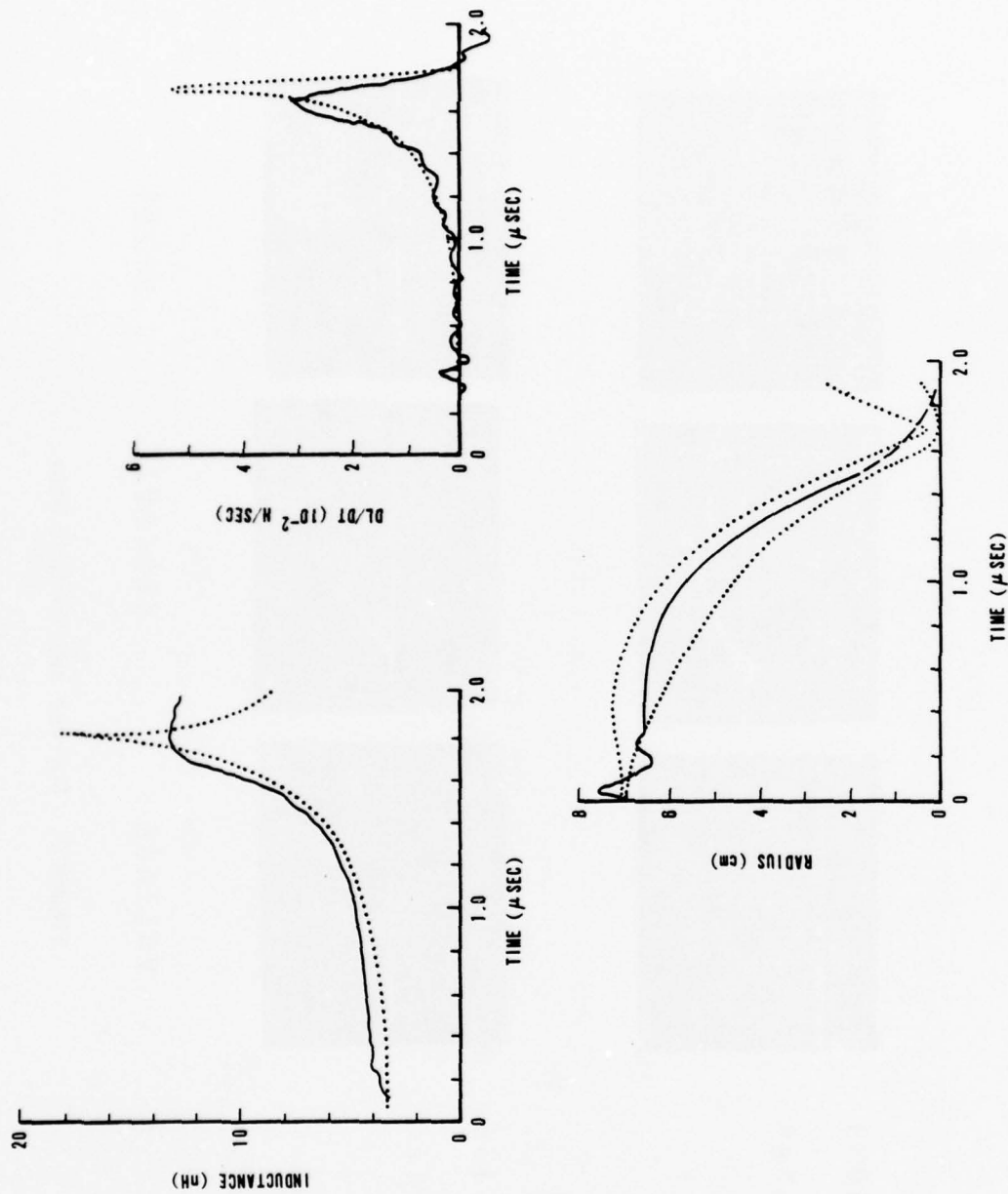ographs which were taken through screen electrodes during the implosion are shown in figure 9. For some shots the main luminous sheath was fairly well defined with a thickness of 1 to 2 cm. A comparison of visible light photographs and laser shadowgraphs indicated that the visible sheath is opaque and that the luminosity was probably from regions close to the ablating electrode. This leads to an ambiguity as to whether the observed light is from the imploding plasma shell or from hot portions of the electrode.

Nevertheless, when photos indicated well-defined, azimuthally symmetric sheaths, the current, voltage, and X-ray data also indicated good implosions. In these cases the position of the luminous front versus time agreed well with the mean current radius versus time and with one-dimensional MHD predictions as shown previously in figure 8. The final implosion velocities inferred from framing and streak photographs (examples of the latter are shown in figure 10) ranged from 15 to 20 cm/μsec. However, the correlation between visible light photographs and load performance was not perfect, since ill-defined, asymmetric luminous sheaths were sometimes observed in shots for which current, voltage, and X-ray data indicated good load performance. Perhaps on such shots hot-electrode ablatants obscured the actual imploding plasma sheath. As is evident in figures 9 and 10, the main sheath was preceded by a light in the center (which began early in the discharge) for foil masses greater than 100 $\mu g/cm^2$. The current associated with the light in the center, i.e., the current inside the main luminous sheath, is typically 10 to 50 KA (<1% of the peak discharge current). Occasionally, luminous streamers or spokes between the main sheath and the center light are evident. These spokes may be near the electrode surface and not part of the imploding sheath.

While the cause of the early center light is not definitely known, it is believed to be due to a pre-pinch involving the ionized residual gas in the electrode gap (density $\sim 10^{-5}$ Torr prior to discharge) and/or a layer

50 ns

VISIBLE LIGHT
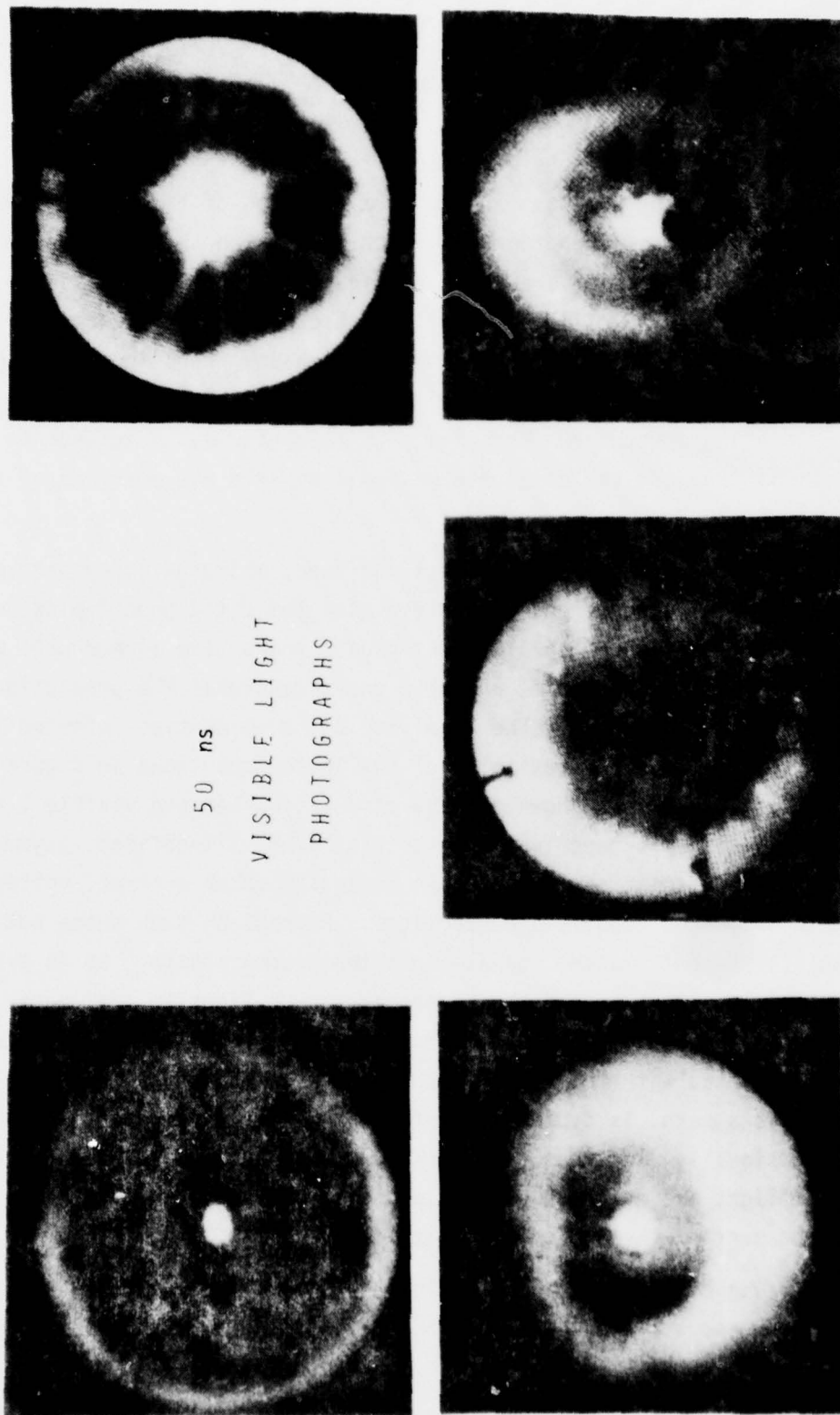
PHOTOGRAPHS

PLASTIC

LOW MASS PLASTIC

ALUMINUM

Figure 9. 50 Nanosecond Exposure Kerr Cell Photos of Implosions.
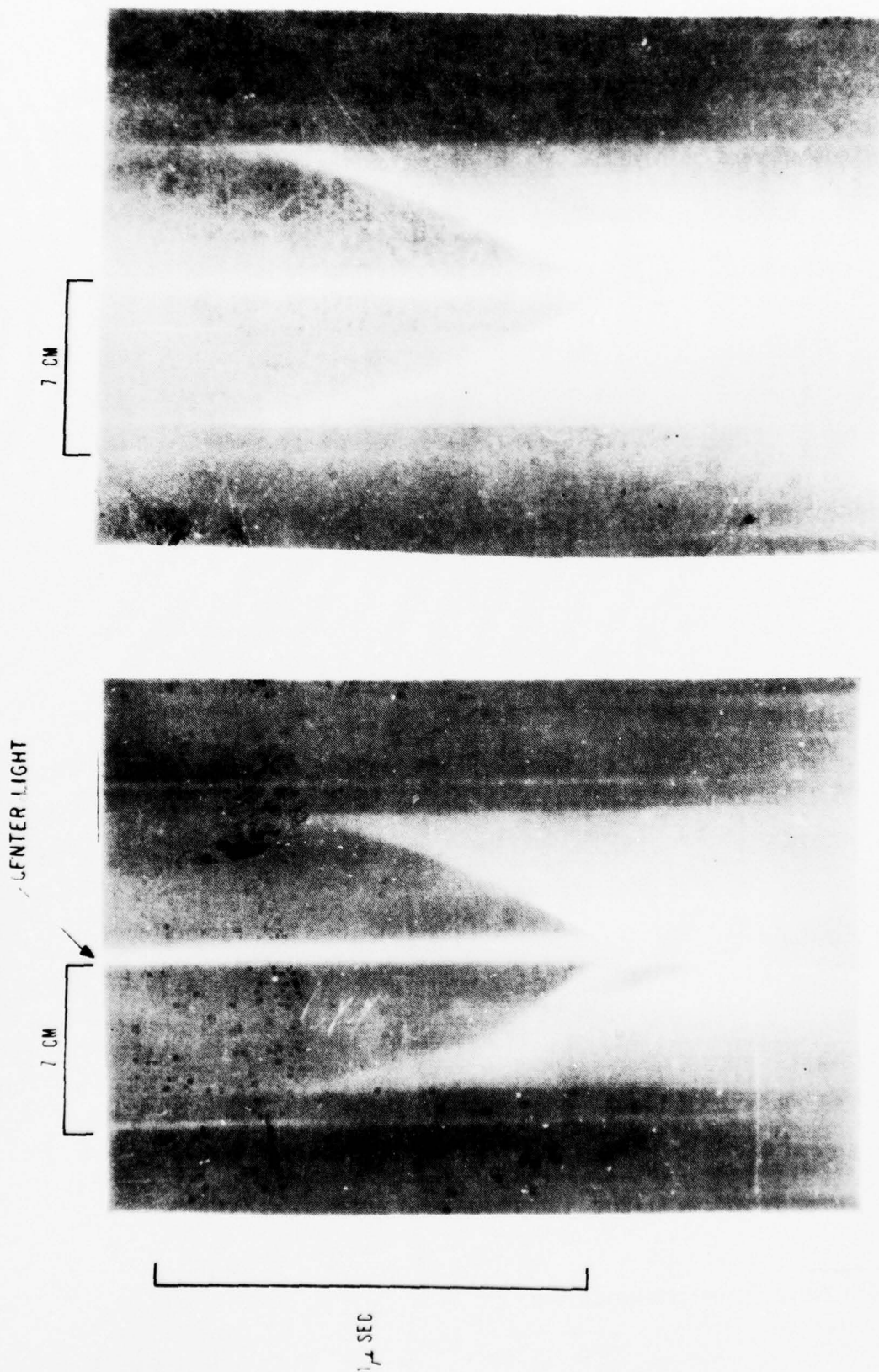
VISIBLE LIGHT STREAK PHOTOGRAPHS

Figure 10.   Streak Photos of Implosions. Image is diameter of perforated
electrode, swept (in image converter camera) for time resolution.

of material from the inner surface of the cylindrical foil.* The early center light is not evident for lower mass foils (40 $\mu g/cm^2$) or for injected gas cylinder implosions (ref. 12), which indicates that the initiation phase plays an important role in the formation of the center light. In experiments to date, the center light appears to have had little effect on the implosion of the main plasma sheath.

---

* Longmire, Conrad (private communication)

SECTION VI

MAGNETIC PROBE DATA

Magnetic probe data was taken for two-load geometries and compared with two-dimensional MHD calculations using code BRAHMA (refs 13, 14). The first data were for MJ implosions of 10.5 cm radius, 1 cm tall, 135 $\mu g/cm^2$ aluminum foils. The calculations assumed solid electrodes while the experiments employed nearly solid electrodes with 3mm diameter access holes for the probes. Magnetic probes were inserted into the electrode gap at radii of 3, 5 and 7 cm, with axial positions ranging from 0.1 to 0.5 cm above the lower electrode. Probes at different radii were azimuthally offset to reduce sheath-probe interaction complications. The probes were single turn, ~ 1 mm^2 and protected by ceramic tubes.

The transient magnetic field measurements obtained from the integrated probe signals are shown in figure 11. Comparison of the absolute values of reversed probes indicated that noise problems were not severe until several hundred nanoseconds after the arrival of the main current sheath. The later arrival and smaller peak field seen experimentally is consistent with a loss of ~ 30 percent of the discharge current at the insulator. The larger precursor or foot (preceding the main rise in the field) seen experimentally, may have been due partly to the center light--prepinch phenomena and partly to a diffuse leading edge to the current sheath. The significant agreement between experiment and calculation is in the shape of the field versus time traces following the first peak. According to the two-dimensional MHD calculations (refs 13, 14), this shape is due to the plasma-electrode interaction. This interaction involves both electrode ablation and heat transfer from the imploding sheath to the electrodes. The heat transfer causes a pressure nonuniformity in the sheath, which in turn causes an axial mass density nonuniformity and results in an $m = 0$ instability near each electrode.

For an ideal discharge the (integrated) magnetic probe signals should be proportional to the total discharge current after the current sheath passes the probe. If electrode ablation is the only complication, the integrated probe signal should exhibit a maximum with the subsequent reduction due to shunting of the discharge current by the ionized ablatants. The more complicated signal seen experimentally and calculationally can be explained in terms
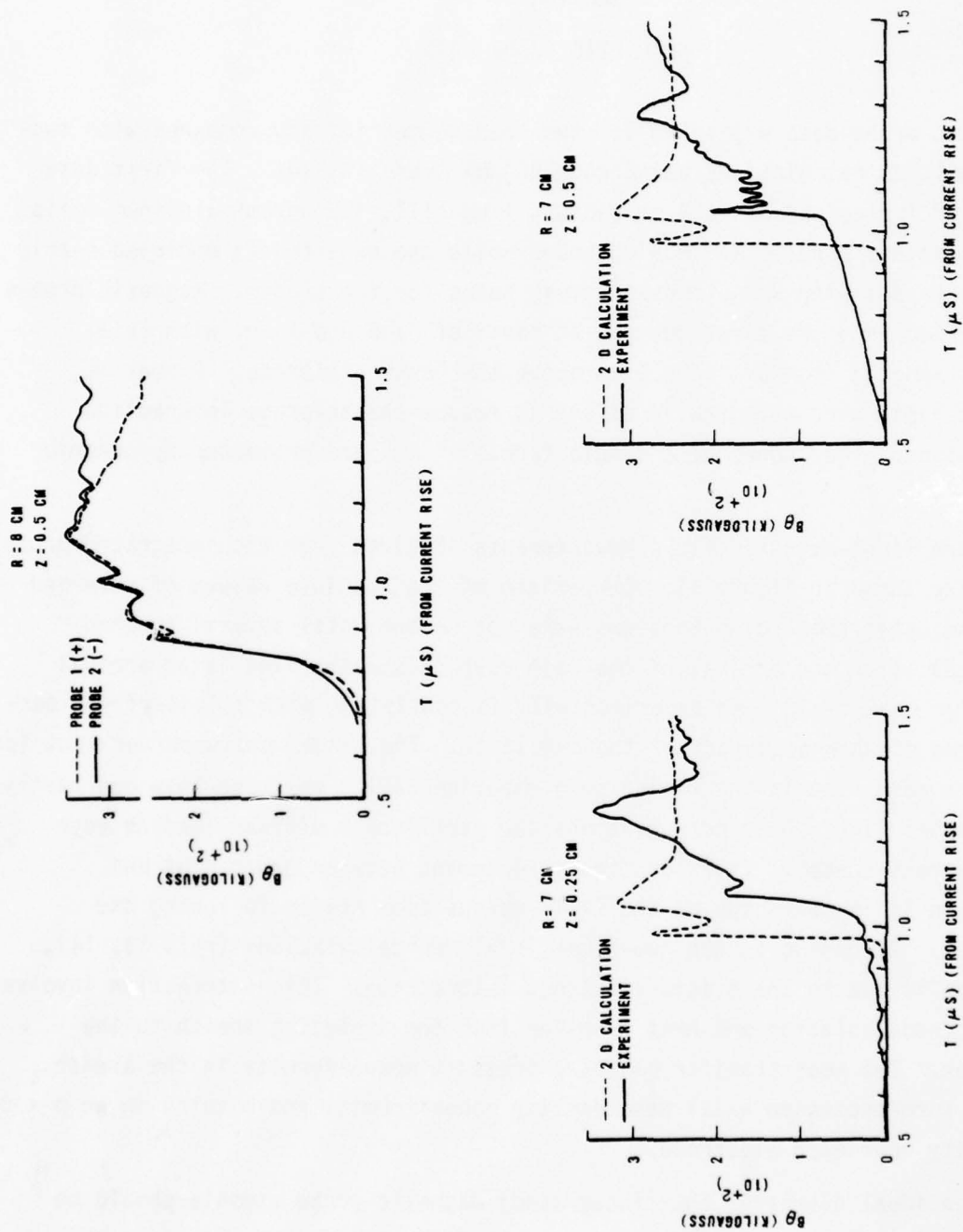
19

Figure 11. Magnetic Probe Data For 10 CM Radius, 1 CM Gap Geometry.

20

of axial-radial structure of the current sheath caused by the heat transfer perturbation just mentioned. Idealized signal traces for the corresponding current sheath structures are illustrated in figure 12.

Magnetic probe data was also taken for the Type C geometry illustrated in figure 4, with 700 kJ discharge energy, to measure the radial distribution of the current density as time, and the current sheath thickness. Five individual magnetic probes sensitive to B_θ were spaced approximately one centimeter apart radially. The probes extended 5mm into the electrode gap (from the grounded-anode side). The current density, calculated assuming azimuthal symmetry, is shown in figure 13 as a function of time and radius. Note that for the early part of the implosion, the current sheath thickness is < the probe spacing (1 cm) and that as the implosion continues, a reversed current appears. The reversed current implies a secondary current path at about 4 cm radius (presumably due to ionized ablatants crossing the electrode gap). Anyway, the leading edge of the current shell continues to implode in a well-defined manner carrying the bulk of the current.

If a secondary current path at the 4 cm radius has occurred, the mean current radius obtained from current and voltage data remains somewhat larger than the radius of the leading edge of the current sheath as indicated by the magnetic probe data.
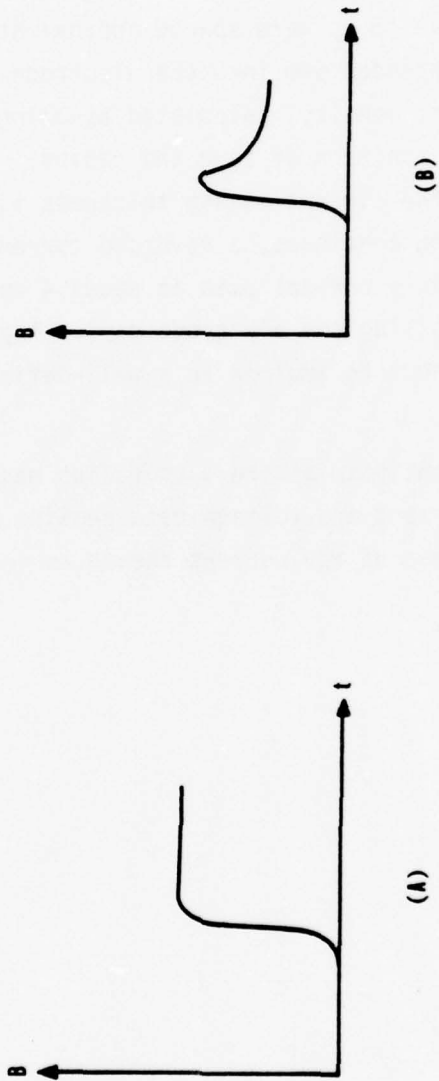
Figure 12. Ideal Magnetic Probe Signals. (A) Ideal discharge (B) When electrode ablation is only complication.
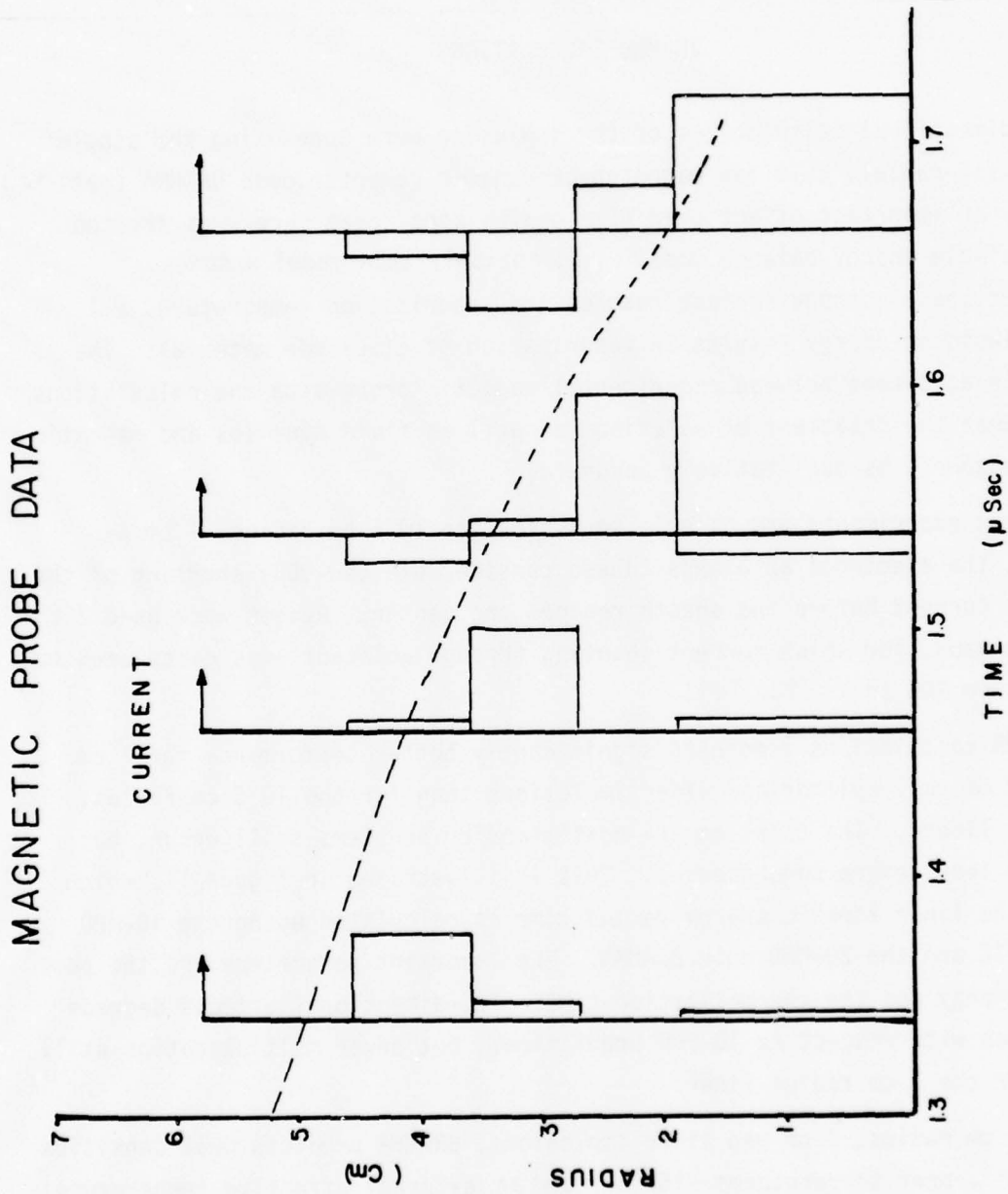
22

Figure 13. Current Distribution Versus Time. Obtained from magnetic probe data for 7 cm radius, 2 cm gap geometry.

SECTION VII

2D-MHD CALCULATIONS

Two dimensional calculations of the implosion were done using the single fluid, axial-radial, Eulerian magnetohydrodynamic computer code BRAHMA (ref. 14). Ablation, an important effect over time scales considered here, was treated using a simple energy balance model*. Essentially this model assumes that after the electrode surface reaches its vaporization temperature, all further incident energy results in vaporization of electrode material. The reasonable agreement between experimental magnetic probe data and calculations suggest that the treatment of ablation (as well as fluid dynamics and magnetic field transport) is qualitatively accurate.

In both experiments and calculations, for the 10.5 cm radius, 1 cm gap geometry, the electrode ablatants caused considerable (50-90%) shunting of the discharge current before the sheath reaches the center. Recent work used 2 cm electrode gaps, for which current shunting through ablatants was calculated to be less than 10% (refs. 13, 14).

BRAHMA calculations predicted significantly better performance for 7 cm radius, 2 cm tall cylindrical liner implosions than for the 10.5 cm radius, 1 cm tall liners. The ablation and heat transfer problems still occur, but with much less severe consequences. This is illustrated in figure 14, which depicts the liner kinetic energy versus time as calculated using the 1D-MHD code MAGPIE and the 2D-MHD code BRAHMA. The important parameters are the peak kinetic energy and the thermalization time. Two-dimensional effects degrade performance with respect to 1D-MHD predictions, but power multiplication still occurs for the 7 cm radius liner.

For 7 cm radius, 2 cm gap liner implosions, BRAHMA predicts peak densities $\sim 10^{22}$ cm^{-3}, peak temperatures ~ 150 eV, and an external effective temperature ~ 40 eV.

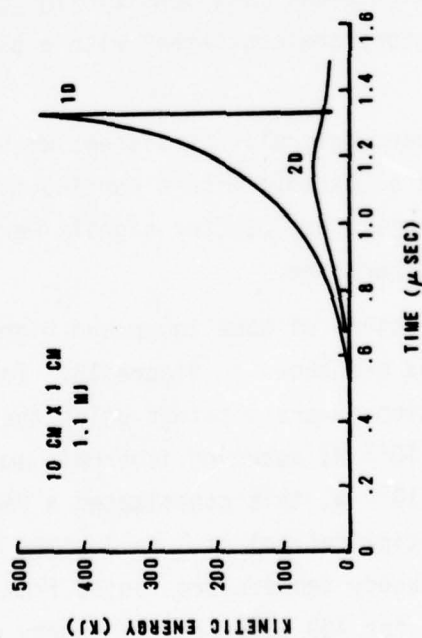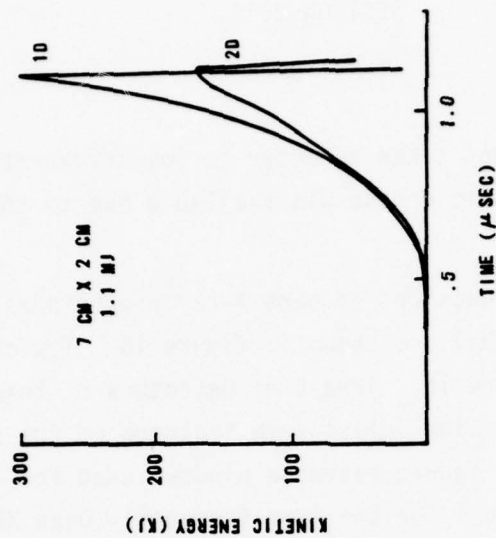* Faehl, R.J., (private communication)

Figure 14. Implosion Kinetic Energy Versus Time As Predicted by 1D and 2D-MHD. Notice the long rise time and rapid decay time for the 7 cm radius geometry. The ratio of rise to decay time is one indicator of the degree of power multiplication.

SECTION VIII

X-RAY DATA

Low-energy X-ray data was taken in order to investigate the thermalized plasma. Only axial diagnostic access was available due to the highly baffled electrode geometry.

The spectral response functions of bare X-ray photodiodes (XRDs) and silicon semiconductor detectors (PINs) are shown in figure 15. Typical filtered XRD responses are shown in figure 16. Arrays of detectors of this type give only approximate spectral information unless some features of the spectral shape are already known. Nominal square response windows used for such approximate analysis are listed in table 1 for the more frequently used XRD. The signal ratios versus blackbody temperature (for assumed blackbody spectral shape) for these XRDs were calculated using code XRADAT* and are shown in figure 17.

Table 2 gives the results for nominal and blackbody assumption interpretation of such an array of XRD signals for an implosion of an aluminized (140Å) Kimfoil ($C_{16}H_{14}O_3$) liner with areal mass density 310 $\mu g/cm^2$. The signal ratios for the lower energy detectors are consistent with a blackbody temperature of about 38 eV.

The detector signals were generally consistent with a low-energy continuum qualitatively similar to a blackbody, with a continuum maximum at ~ 80 to 150 eV photon energy. On some shots, the detector signals were in approximate agreement with a single blackbody temperature.

Examples of the time history of some lower and higher energy XRD signals taken for 700 kJ discharges are shown in figure 18. The FWHM is generally $\lesssim 100$ ns. The X-ray emission powers obtained using the lower energy XRDs are typically ~ 0.5 to 1.0×10^{12} W, assuming isotropic emission. Since the electrical delivery power was $\sim 0.5 \times 10^{12}$ W, this constituted a radiation to electrical power ration (or power multiplication) of 1 to 2. The yields ranged from 50 to 100 kJ(total) and the blackbody temperature ranged from 30 to 50 eV. In general, the highest yielding shots for 700 kJ discharge energy were those using 7 cm radius, aluminum coated 300 $\mu g/cm^2$ Kimfoil liners.

---

* Johnson, D.J., (private communication)
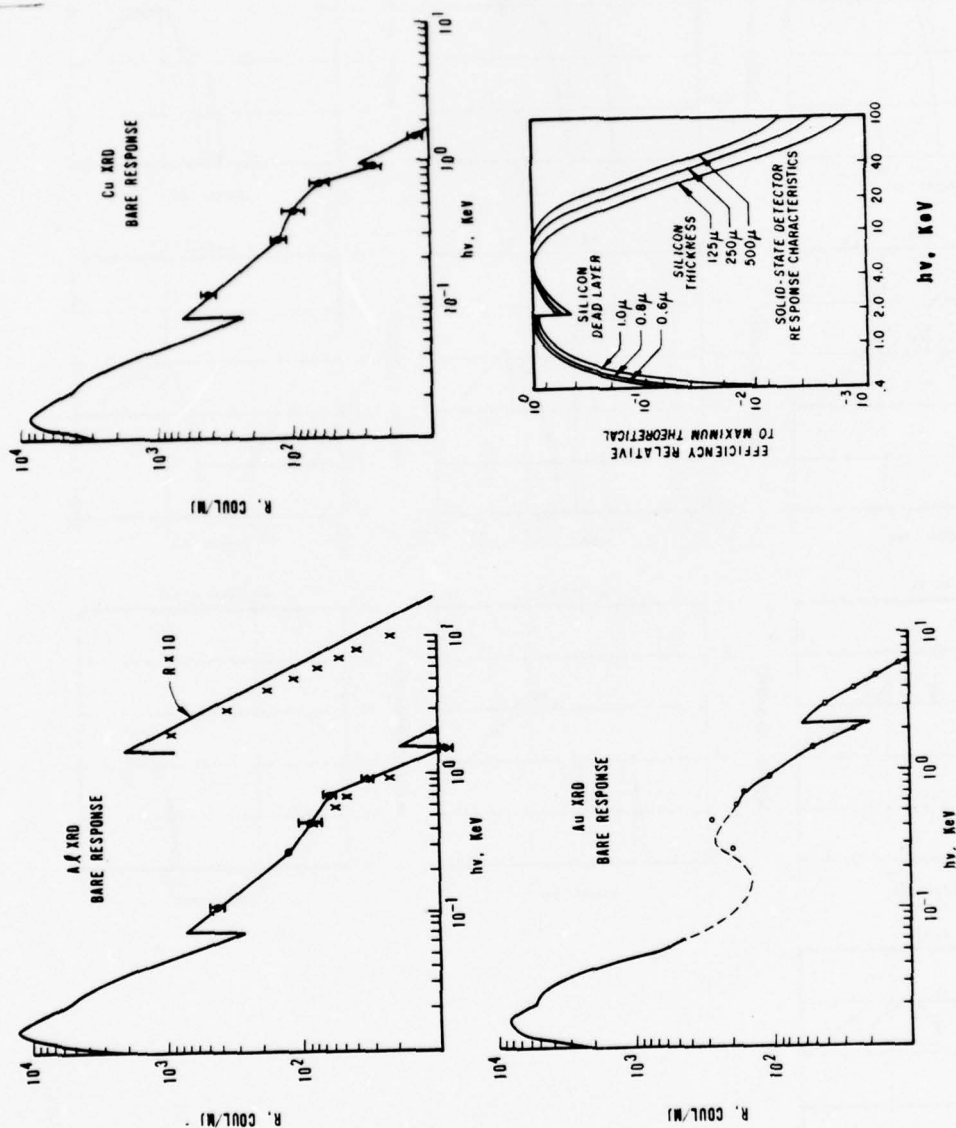
Figure 15. Unfiltered X-Ray Diode and Si-PIN Response Functions. The low energy XRD data is that of Cairns and Samson (ref. 15). The XRD data from 109 to 1490 eV photon energy is that of Burns and Day (ref. 16)(I) and J.L. Gaines et al. (ref. 17)(0). The data for greater than 1490 ev is that of J.L. Gaines et. al., and P.B. Lyons (private communication).

27

Figure 16. Filtered X-Ray Diode Response Functions. Cathode and filter materials identified in figure. For example, CU/FV means Cu cathode and Formvar anode. FV is 75 $\mu g/cm^2$ $C_5H_7O_2$. KF (kimfoil) is 250 $\mu g/cm^2$ $C_{16}H_{14}O_3$.

Table 1

X-RAY DIODE RESPONSE WINDOWS

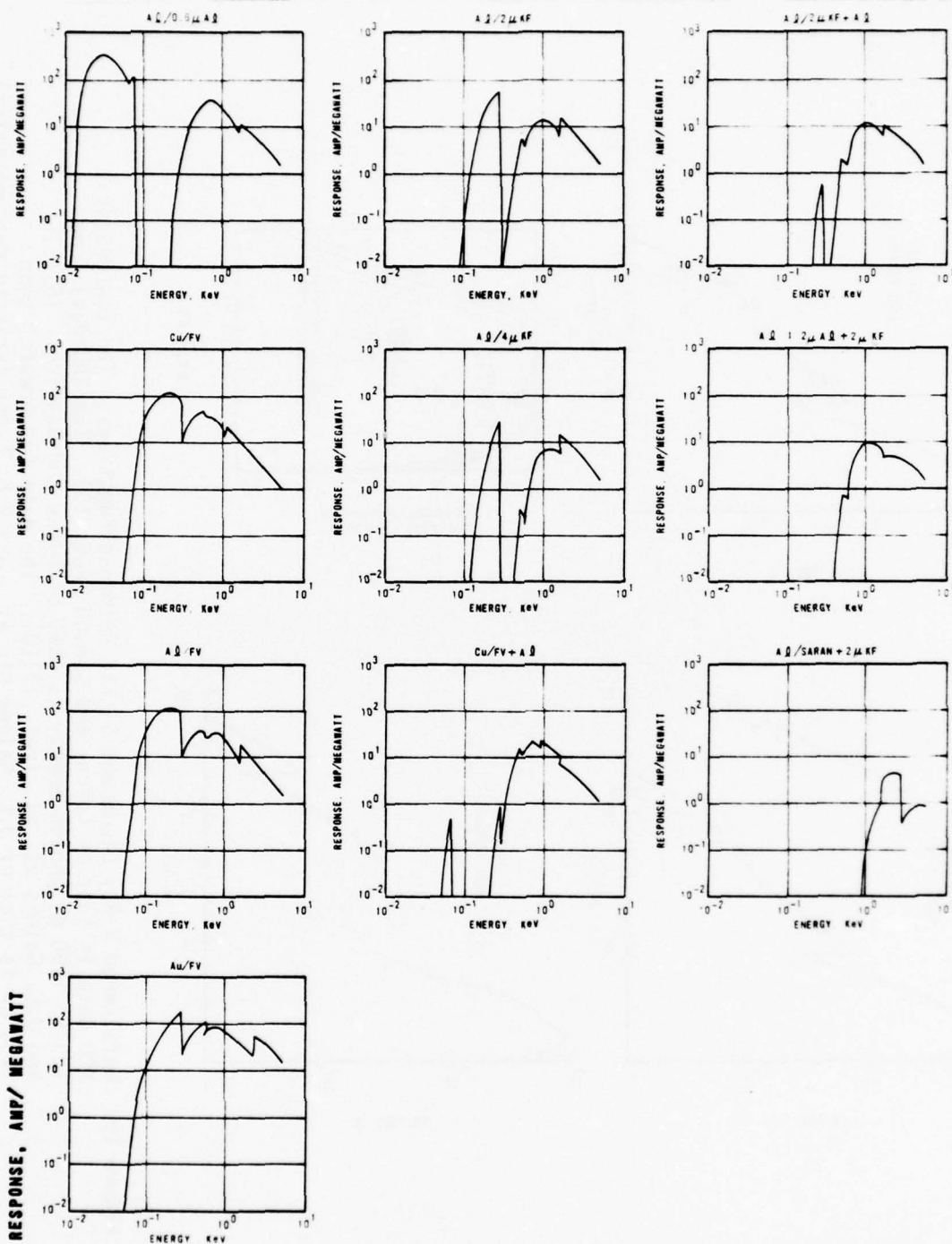| CATHODE	FILTER	R_p	E_p	$R_{NOM}(\pm$ FACTOR)	E_1-E_2
CU	FV	108 C/MJ	202 EV	36 C/MJ ($\pm$ FAC. 3)	>86 EV
CU	0.6 μAL+FV	22.6 C/MJ	712 EV	7.5 C/MJ ($\pm$ FAC. 3)	>350 EV
AU	FV	198 C/MJ	280 EV	66 C/MJ ($\pm$ FAC. 3)	>114 EV
AL	0.6 μAL	342 C/MJ	31 EV	170 C/MJ ($\pm$ FAC. 2)	15-74 EV
AL	2 μKF	58 C/MJ	280 EV	19.3 C/MJ ($\pm$ FAC. 3)	140-280 EV
AL	FV	109 C/MJ	202 EV	36 C/MJ ($\pm$ FAC. 3)	>86 EV
AL	4 μKF	27.3 C/MJ	280 EV	9.1 C/MJ ($\pm$ FAC. 3)	185-280 EV
AL	2 μKF+0.6 μAL	11.4 C/MJ	910 EV	3.8 C/MJ ($\pm$ FAC. 3)	>500 EV
AL	2 μKF+1.2 μAL	9.3 C/MJ	1.21 KEV	3.1 C/MJ ($\pm$ FAC. 3)	>600 EV
AL	0.5 MIL SARAN + 2 μKF	4.57 C/MJ	2.1 KEV	4.0 C/MJ ($\pm$ 15%)	1.56-2.82 KEV

Peak responses (R_p) at energy E_p and nominal "square" response windows are shown for frequently used X-ray diode cathode/filter combinations. FV is 75 μg/cm^2 $C_5H_7O_2$ (Formvar). 2μKF is 250 μg/cm^2 $C_{16}H_{14}O_3$ (Kimfoil). The factor of 3 error is conservative. In general, the errors for realistic spectra (e.g., black body) are factors ~1-2. C/MJ is Coulomb/Mega Joule which is the same as Ampere/Mega Watt. The 0.5 mil Saran plus 2μ KF filter consists of 58 μg/cm^2 H, 780 μg/cm^2 C, 1540 μg/cm^2 CL, and 49 μg/cm^2 O.
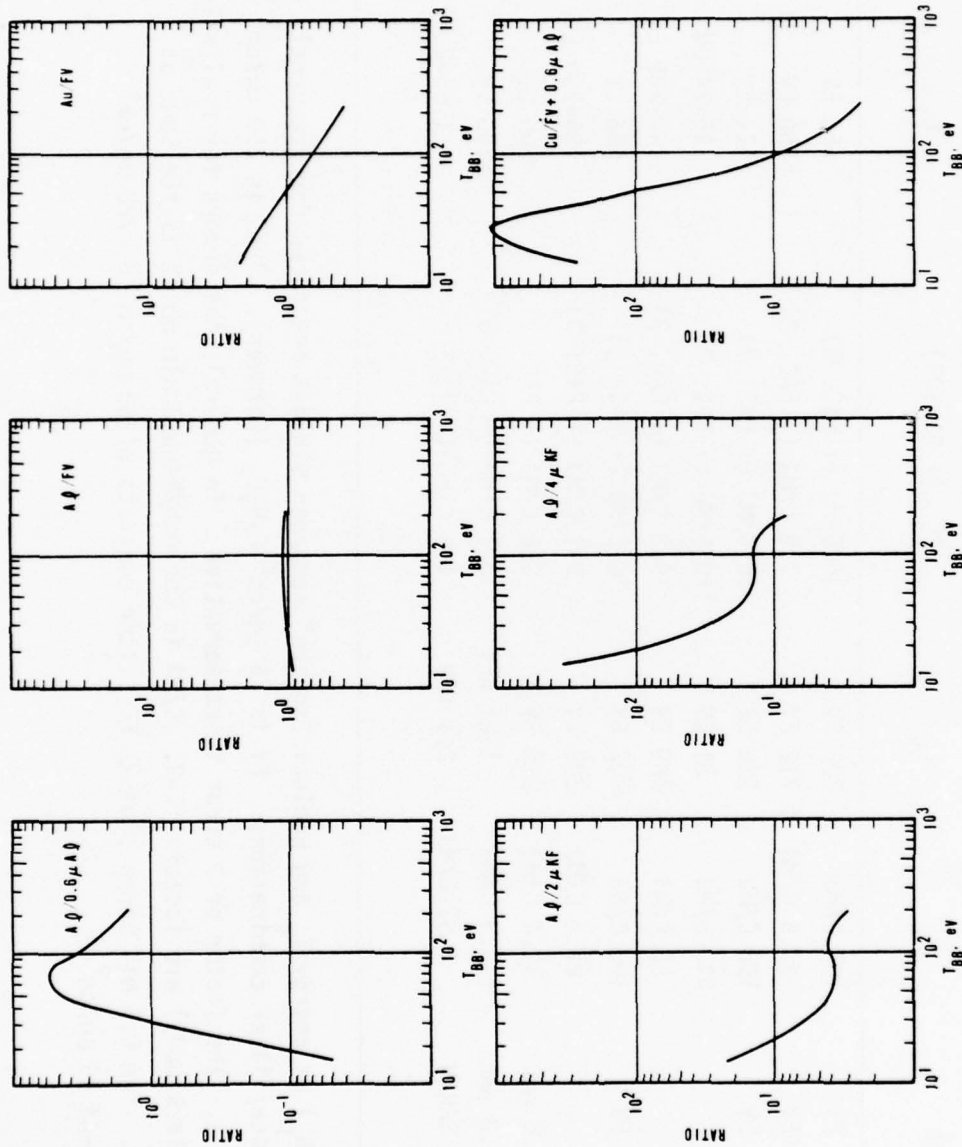
Figure 17. Ratio of Detector Signals Versus Black Body Temperature. Plots show calculated ratios of Cu/FV to other X-ray diode signals versus radiation temperature for assumed black body spectral shape.

Table 2

X-RAY DIODE DATA FOR REPRESENTATIVE SHOT

X-Ray Diode	E_1-E_2	$P_{NOM}(E_1 \rightarrow E_2)$	T_{BB}	$P_{BB}(T_{BB}$ = 38 eV)
Al/KF + 1.2 µAl	>630 eV	1.78×10^9 W	50 eV	
Al/KF + 0.6 µAl	>500 eV	2.42×10^9 W	40	
Cu/FV + 0.6 µAl	350 eV	1.48×10^{10} W	44	
Al/FV + 2 KF	185-284 eV	7.69×10^{10} W	38	0.43×10^{12} W
Al/FV + KF	140-284 eV	1.70×10^{11} W	42	0.52×10^{12} W
Au/FV	>114 eV	2.63×10^{11} W	38	0.43×10^{12} W
Cu/FV	>86 eV	6.63×10^{11} W		0.43×10^{12} W
Al/FV	>86 eV	6.30×10^{11} W		0.41×10^{12} W

X-ray diodes are identified as in Figure 16 and 17. E_1-E_2 are the boundaries of the nominal response windows (cf. Table 1). P_{NOM} ($E_1 \rightarrow E_2$) is the estimated X-ray emission power from photon energies E_1 to E_2, using the nominal response functions to interpret the signals. T_{BB} is the black body temperature which agrees with the ratio of the X-ray diode signal to the Cu/FV X-ray diode signal, assuming a black body spectral shape. The lower energy detector signals are consistent with a 38 eV black body. P_{BB} is the (total) radiation power indicated by the detector signal for an assumed 38 eV black body spectrum. Isotropic emission is assumed.

AL/SARAN
XRD

500 NANOSECONDS/DIV

Cu/FV
XRD

Cu/FV
XRD

AL/FV
XRD

100 NANOSECONDS/DIV
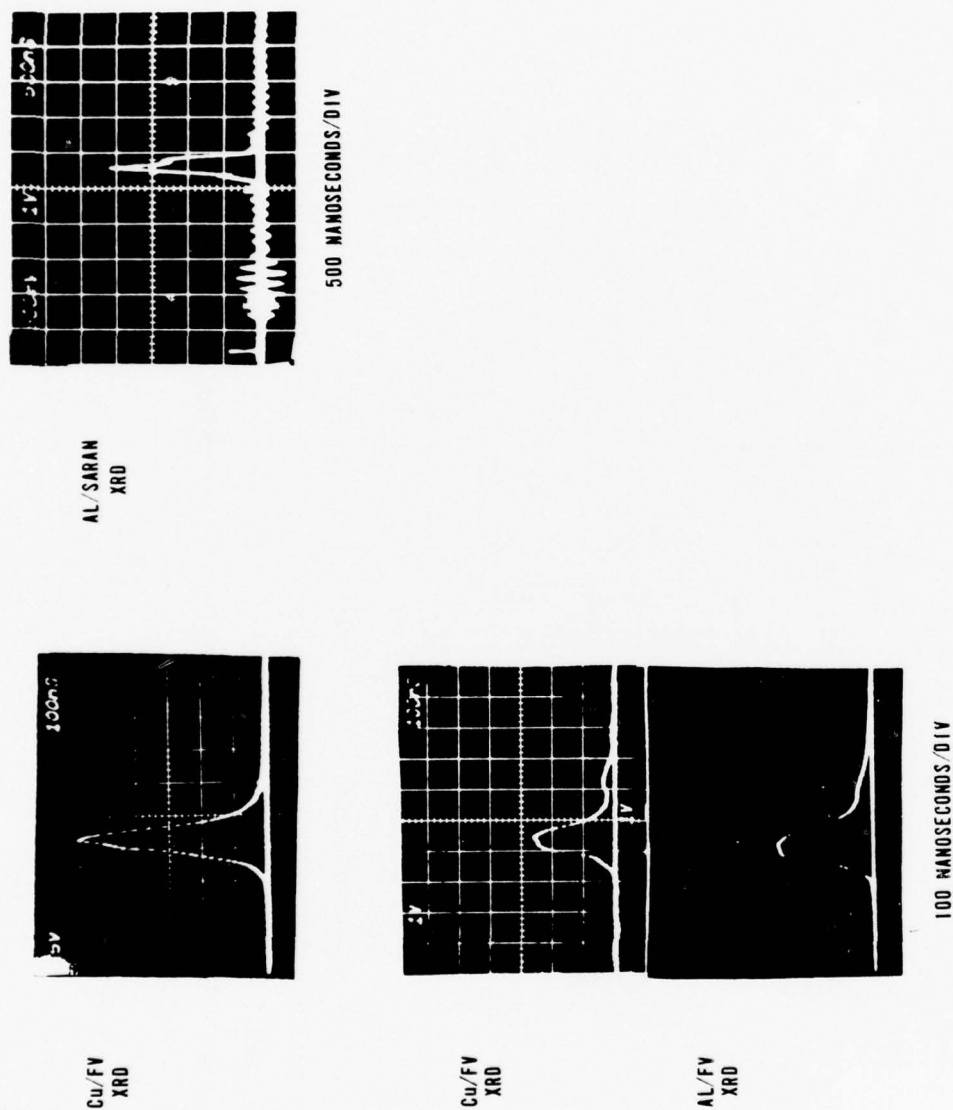
Figure 18. Representative X-Ray Diode Signals. The signal on the right was obtained using an XRD sensitive to > 1.56 kev photons. The signals on the left were obtained using low energy XRDs sensitive to >80 ev photons. Notice the nearly identical Cu/FV and Al/FV signals at the lower left of the figure. These were obtained on the same shot, and the similarity is expected since the response functions are very similar for photon energies below 500 eV.

While the low-energy X radiation was approximately consistent with a 30 to 50 eV blackbody, the higher energy radiation (photon energy > 1 keV) consisted largely of Al line and recombination radiation. The $Al^{11+}(1S^2 - 1Snp)$ and Al^{12+} (1S-np) series were consistently observed using Potassium Acid Phthalate (KAP) and Rubidium Acid Phthalate (RAP) bent crystal spectrometers. A densitometer trace with line identifications is shown in figure 19. The recombination continuum is characterized by temperatures as high as 400 eV (ref. 18). The X-ray yields observed above 1 kev ranged from 100 to 200 J for aluminized plastic liners to 1 to 4 kJ for 200 $\mu g/cm^2$ aluminum liners.

Typical PIN signals, which are generally saturated, are shown in figure 20. The PINs, used in a helium atmosphere and filtered by a 4 mil Be vacuum window, were sensitive to > 2 keV X rays.

Some lower energy bent crystal data (obtained using Lead Stearate bent crystal with 1/8-inch radius of curvature) is shown in figure 21. The higher order lines are deleted. The Al^{11+} ($1S^2 - 1S2p$) resonance and intercombination lines have been seen in orders 2, 3, 4, 5, 6 and 7 (in an Al liner implosion). The O^{7+} (1S-2P) line has been seen in orders 1, 2, 3 and 4 (in plastic liner implosions). Two lines (believed to be first order) at energies 234 and 254 eV have been consistently observed in both Al and aluminized plastic liner implosions. Tentative identifications for these lines are Al^{10+} (3d-2p) and Al^{10+}(3p-2s). Except for these two lines, the radiation spectrum from 150 to 280 eV appears to be dominated by continuum. Comparison of the absolute yield for photon energies from 150 to 280 eV obtained from Lead Stearate data with that obtained using an aluminum cathode, 2μ thick Kimfoil ($C_{16}H_{14}O_3$) filtered XRD gives factor of two agreement. The disagreement may be due in part to differences in individual crystal reflectivities (factor of 2). The degree of agreement gives some confidence in the use of XRDs at low photon energy.

Some representative X-ray pinhole camera photos are shown in figure 22. The pinholes were 50 to 100 μ in diameter (measured by Fraunhoffer diffraction). The lowest energy cameras used to date used two layers of aluminized (140 Å) 2 μ thick Kimfoil ($C_{16}H_{14}O_3$) filters and Kodak RAR2490 film, with sensitivity windows ~200 to 280 eV and $\gtrsim 500$ eV. Sometimes the radiating region (as viewed axially) was donut shaped, with an outer diameter somewhat less than the electrode hole diameter (2 cm) and an inner diameter of less than 1 cm. Sometimes the radiating region was donut shaped with a separate central hot spot, and sometimes there was only a central hot spot. The smallest radiating sources

KAP Crystal Spectrometer
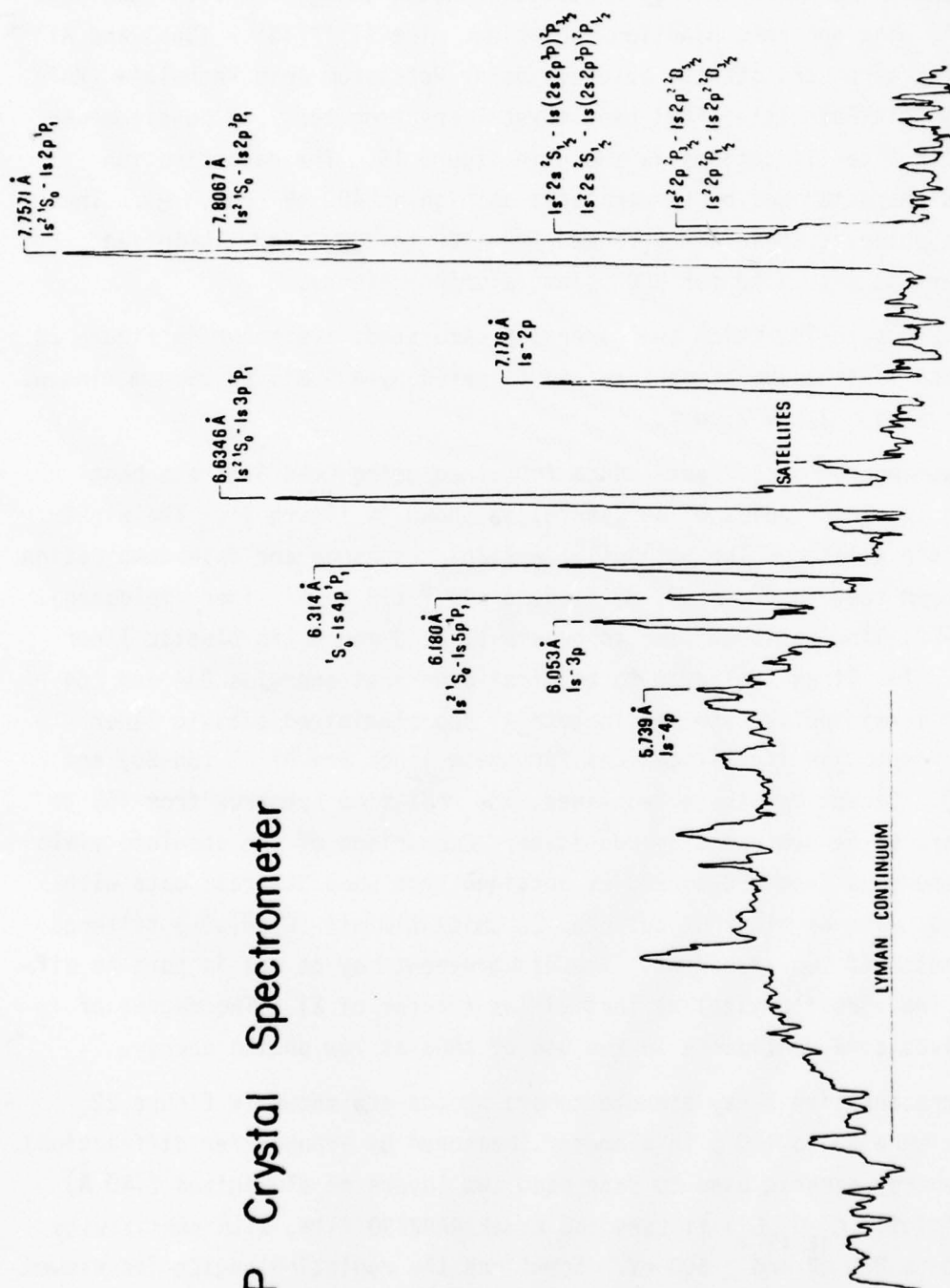
Figure 19. KAP Convex Curved Crystal Spectrograph Data. This shows Al[11+] and Al[12+] lines and recombination radiation from 1.6 to 3 kev. Energy increases from right to left in this figure. The KAP reflection efficiency used to interpret such data was that of Chase et. al. (ref. 19) and the (Medical No Screen) film response used was that of Dozier, et. al. (ref. 20). Further discussion is in text and in ref. 18.
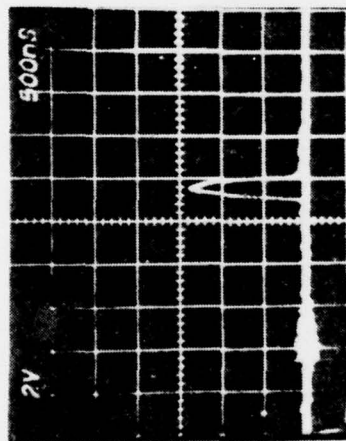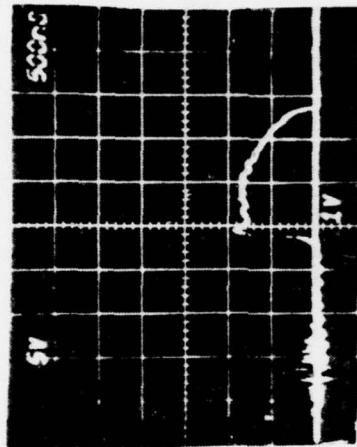
PIN SIGNALS

Figure 20. Representative Si Pin Detector Signals.

35

LEAD STEARATE BENT CRYSTAL SPECTRUM
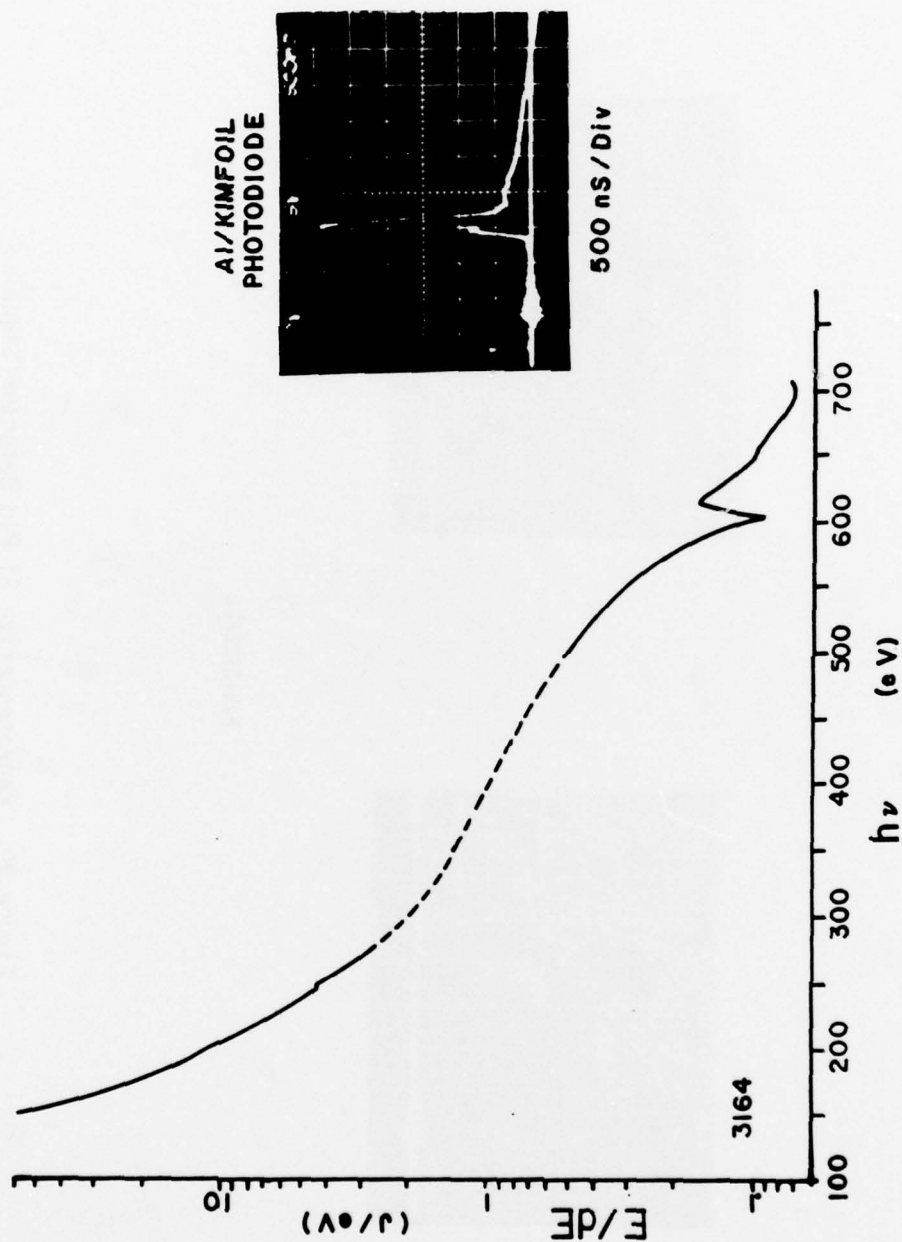
Figure 21. Lead Stearate Convex Curved Crystal Spectrograph Data. Data was obtained using 0.125 inch radius crystals provided by B. L. Henke. The Kodak RAR2490 film response of Benjamin, Day, and Lyons (ref. 21) and the crystal reflectivity reported by B. L. Henke (ref. 22) were used to interpret the data. Further discussion in text.

36
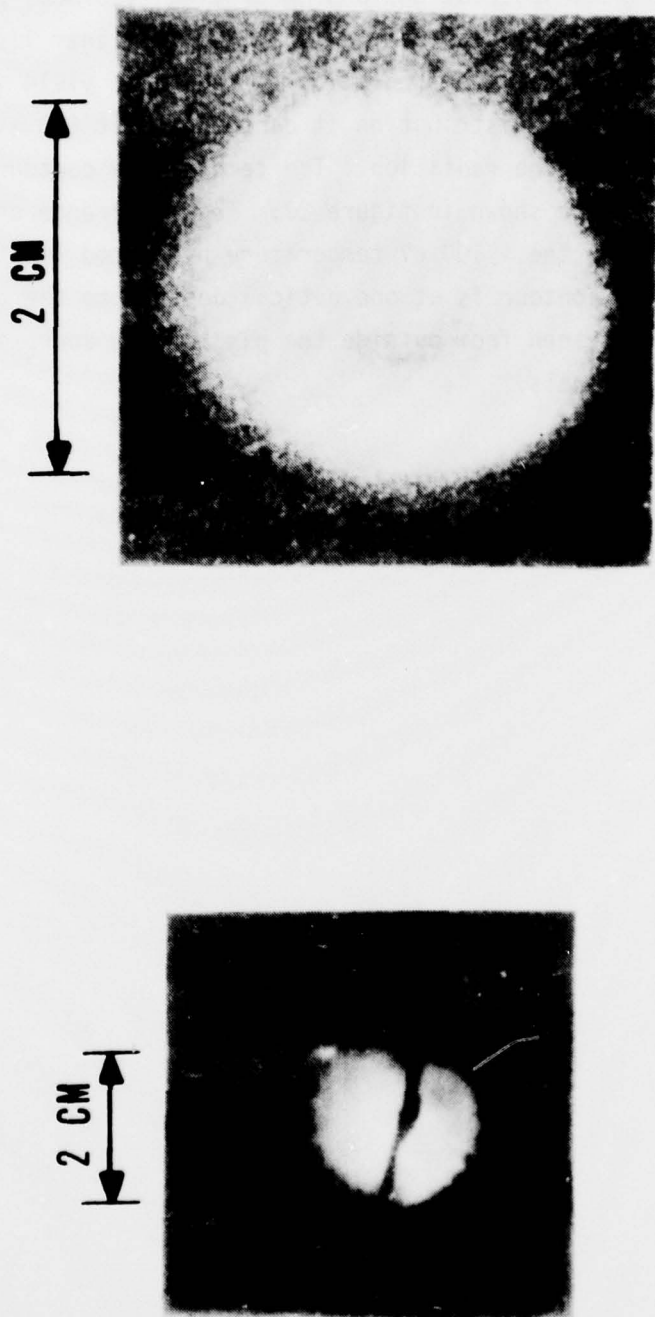
X-RAY PINHOLE CAMERA PHOTOS

Figure 22. X-Ray Pinhole Camera Photos. The photo on the left indicates a 0.5-0.7cm diameter X-ray source. The dark line is the shadow of a probe support about 5 cm outside the electrode gap. This photo was sensitive to photons in the energy ranges 200-280 eV and 500 eV. The photo on the right, sensitive to > 1 kev photons, shows a central radiating region surrounded by a donut shaped radiating region which is inside the electrode center hole.

observed to date have had a diameter 5mm. The differences in spatial distribution are not obviously correlated with other X-ray measurements (yield, power, or temperature).

The comparison of experimental observations and theoretical (2D-MHD) predictions* of the X-ray output for a 7cm radius 2cm tall, 200 $\mu g/cm^2$ liner implosion are summarized in table 3. Since the code prediction of radiation yield is based on the calculated plasma temperature distribution it cannot predict the experimentally observed Al^{11+} and Al^{12+} line radiation. The temperature contours for the "hottest" time in the pinch are shown in figure 23. The occurrence of Al line radiation is consistent with the > 100 eV temperature predicted for the center of the pinch. The 40 eV contour is at one optical depth into the pinch, and the predicted temperature as seen from outside the pinch is in approximate agreement with low-energy XRD signals.

---

* Roderick, N.F. and T.W. Hussey (private communication)

Table 3

2D-MHD CODE PREDICTIONS VERSUS EXPERIMENTAL RESULTS
FOR X-RAY YIELD AL LINER IMPLOSION

	2D-MHD	EXPERIMENT
Total Yield	100 KJ	50-100 KJ
FWHM	90 NS	80-100 NS
PLASMA TEMPERATURE	40 EV	30-50 EV

2D MHD CODE PLASMA TEMPERATURE CONTOURS
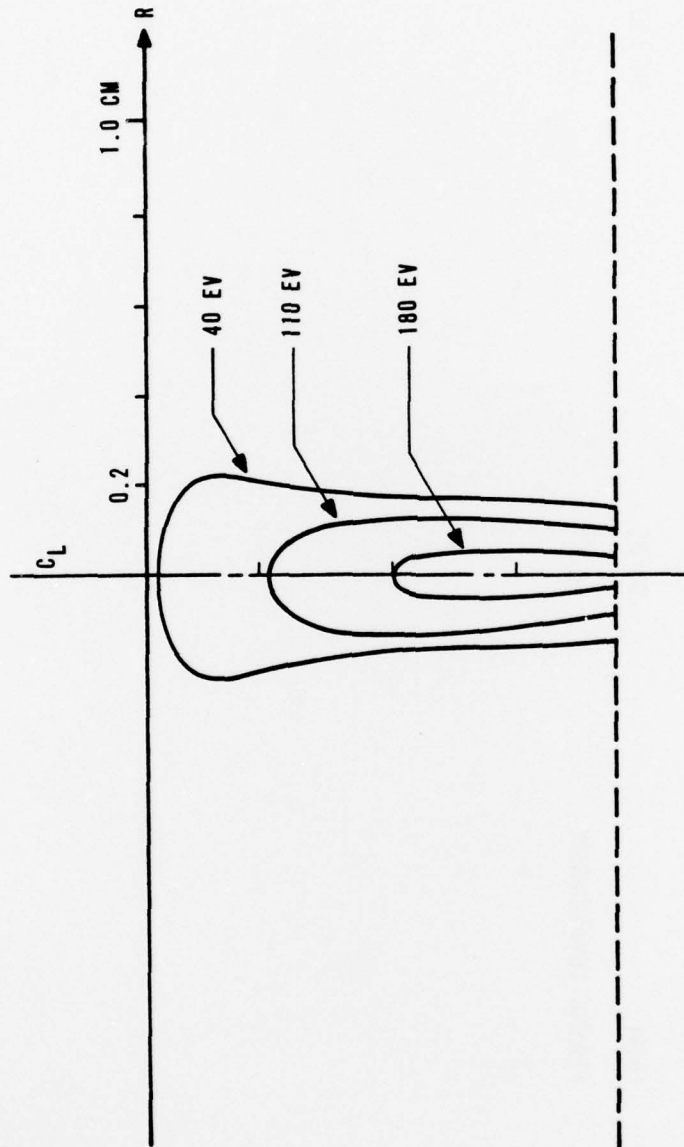
HIGH ENERGY (AL^{11+}, AL^{12+}) RADIATION EXPERIMENTALLY OBSERVED IS CONSISTENT WITH HOT (~150 EV) CORE PREDICTED BY BRAHMA.

Figure 23. Radiation Temperature Contours as Predicted by 2D-MHD. The BRAHMA predictions of radiation temperature contours at the hottest time in the pinch are shown for one-half of the electrode gap. The predictions are for a 200 $\mu g/cm^2$ Al liner implosion. The hot core temperature predicted by BRAHMA is consistent with the occurrence of the experimentally observed Al^{11+} and Al^{12+} lines.

SECTION IX

DISCUSSION

The experimental results indicate that fairly high-energy liner implosions have been achieved, resulting in 50 to 100 kJ, 100 ns X-ray bursts, which is consistent with 2D-MHD (BRAHMA) predictions Optical and magnetic probe data agree qualitatively with BRAHMA predictions on the radial-axial structure of the imploding liner sheath. The agreement between BRAHMA predictions and experimental results suggest that BRAHMA is a very useful design tool.

The observed radiation was consistent with an 30 to 50 eV quasi blackbody with additional higher temperature and optically thin components. The experimental radiation powers of 0.5 to 1.0×10^{12}W assuming isotropic emission, constitute a power multiplication of 1 to 2 over electrical input.

The power multiplication can, in principle, be improved by achieving sharper, more symmetric imploding liner sheaths in the final stage of the implosion and/or by using larger radius, lower mass liners. The degree of improvement conceivable is indicated in table 4. The table entries were calculated using a circuit solver code (DELORES)*, with the assumed sheath thickness and current cutoff radii indicated. For the 7 cm radius liner, the calculations, with 2 cm sheath thickness and current cutoff radius agree reasonably well with BRAHMA predictions and experiment.

The possible problems in trying larger radius, lower mass liner experiments are Rayleigh-Taylor instabilities (due to higher acceleration) and practical difficulties in handling liners with low areal mass density. The instability problems may be alleviated by one of several sheath stabilization procedures under consideration. These procedures include electrode shaping (using an electrode gap which varies with radius), injection of axial magnetic field prior to the implosion discharge, using two or more concentric liners (i.e, staging), and prevaporization of the foil liner to reduce the radial density gradient of the liner. An approach which might alleviate both low areal mass density and sheath stabilization problems is to use an injected gas liner, perhaps with preionization prior to the implosion discharge.

---

* Clark, J.G. (Private Communication)

Table 4

Implosion Predictions

R_0	dM/dA	$\Delta R = 1$ cm			$\Delta R = 2$ cm	
		t_p	KE	P	KE	P
20 cm	5 $\mu g/cm^2$	1.25 μsec	230 KJ	13.8 TW	198 KJ	5.6
	10	1.53	285	17.7	250	5.5
	20	1.88	318	13.0	296	5.0
14	10	1.13	187	8.6	161	3.4
	20	1.37	238	8.8	201	3.4
	50	1.79	307	8.1	264	3.3
7	75	1.10	152	3.3	110	1.01
	150	1.33	198	3.4	145	1.09
	300	1.62	245	3.3	177	1.04

Slug model predictions of implosion kinetic energy (KE) and kinetic to thermal energy conversion power (P) for assumed sheath thickness and current cutoff radius ΔR. R_0, dM/dA, and t_p are the initial liner radius, areal mass density of the foil liner, and implosion time. The circuit parameters used in the calculations were C = 222 μf, initial inductance = 6.5 nanohenries, circuit resistance = 1 mΩ and initial voltage = 80 KV. The electrode gap is 2 cm.

42

The main thrust of the present imploding liner development effort is to achieve sheath stabilization and large radius, low mass implosions, with the hope of achieving increased performance levels. In the future it may be possible to use explosive magnetic flux compression generators (ref. 23) to drive foil cylinder liners (ref. 1). Further experiments are intended to investigate the imploding liner concept and to provide scaling information for the design of explosive generator driven liners, for which delivered energy $\sim 10^8$ J and plasma formation powers $\sim 10^{15}$ W, are conceivable (ref. 1).

ABBREVIATIONS, ACRONYMS AND SYMBOLS

Al	Aluminum
B	Magnetic field intensity
Be	Beryllium
BRAHMA	A two dimensional MHD Computer Code
C	Carbon
cm	Centimeter
DELORES	An imploding liner circuit computer code
eV	Electron volt
FWHM	Full width at half maximum
H	Hydrogen
h	Electrode gap (height)
I	Discharge current
J	Current density
JxB	Vector product of current density and magnetic field
KA	Kilo-ampere
KJ	Kilo-joule
KV	Kilo-volt
KAP	Potassium acid Phthalate
MA	Mega-ampere
MAGPIE	A one-dimensional MHD computer code
MHD	Magneto hydro dynamic
MJ	Mega-joule
ns	Nanosecond
O	Oxygen
PIN	Positive-Intrinsic-Negative semi-conductor junction

R	Electrical resistance of discharge
RAP	Rubidium acid phthalate
r(t)	Imploding liner radius as function of time t
SHIVA	Name of imploding liner program at Air Force Weapons Laboratory
t	time
u(t)	Implosion velocity as function of time t
UV	Ultraviolet
V	Discharge voltage
XRADAT	Computer code which calculator detector response functions
XRD	X-Ray diode
$\overset{o}{A}$	Angstrom
I	dI/dt (time rate of change of current I)
L	dl/dt (time rate of change of inductance L)
μ	Micron
μ_0	Magnetic permeability
μs	Microsecond
π	pi

REFERENCES

1. Turchi, P.J., and Baker, W. L., "Generation of High Energy Plasmas by Electromagnetic Implosion," J. Appl. Phys. 44, 4936 (1973).

2. Ch. Maisonnier, "Hollow Dynamic Pinch," Plasma Physics and Controlled Nuclear Fusion, Vol II, p. 345-365. International Atomic Energy Agency, Vienna, 1966.

3. Alikhanov, S. G., "The Production of Pulsed Megagauss Fields by Compression of the Metallic Cylinder in Z Pinch Configuration," J. Sc. Inst. (J. Phys. E.) (1968).

4. Kalitkin, N.N., and Tsareva, L. S., "Approximate Theory for amplification of Magnetic Fields," Soviet Physics, Technical Physics, 14, 1050 (1970).

5. Baker, W. L., Reinovsky, R.E., et.al., "Progress in Foil Imploding Liner Plasma Generation," Am Phys, Soc 21, 1054 (1976)

6. SHIVA One Megajoule Capacitor Bank, AFWL-TR-75-271, Air Force Weapons Laboratory, Kirtland AFB, NM, (1975).

7. Leonard, S. L., Chapter 2 in "Plasma Diagnostic Techniques," edited by Huddlestone, R.H. and Leonard, S.L., Academic Press (1965).

8. Lovberg, R. H., Chapter 3 in "Plasma Diagnostic Techniques," by Huddlestone, R. H., and Leonard, S.L., Academic Press (1965).

9. Johnson, D. J., Two Systems for Measurement of High Intensity Vacuum Ultraviolet Plasma Radiation, AFWL-TR-74-43, Air Force Weapons Laboratory, Kirtland Air Force Base, New Mexico, (1974).

10. Johnson, D. J., "An X-Ray Spectral Measurement System for Nanosecond Plasmas," Rev. Sc. Inst. 45, (1974).

11. Steinberg, D., "A One Dimensional Magnetohydrodynamics Code," UCRL 14931, Lawrence Livermore Laboratories, California (1966).

12. Degnan, J. H., Reinosvky, R. E., et. al., "Studies of High Energy Density Plasma Generation by Cylindrical Gas Shell Implosion," IEE International Conference on Plasma Science, 65 (1976).

13. Clark, M.C., "Magnetic Field Measurements on a Current Driven Plasma Implosion," Am. Phys. Soc. 21, 1054 (1976).

14. Baker, W. L., et. al., SHIVA Phase II Electromagnetic Implosion Research, AFWL-TR-74-307, Air Force Weapons Laboratory, Kirtland AFB, New Mexico. (1974).

15. Cairns, R. B. and Samson, J.A.R., "Metal Photocathodes as Secondary Standards for Absolute Intensity Measurements in the Vacuum Ultraviolet," J. Opt. Soc. Am. 56, 1568 (1966).

16. Burns, E.J.T., and Thurston, J. F., "The Use of Some Metal Photocathodes for Absolute Intensity Measurements in the Soft X-Ray Vacuum Ultraviolet," Appl. Spect. 31, 317 (1977).

17. Gaines, J. L., and Ernst, R. D., "X-Ray Detector Calibrations in the 183 to 932 eV Energy Range," UCIR-1075, Lawrence Livermore Laboratory California, (1976).

18. Burns, E.J.T., et. al., "Soft X-Ray Spectroscopy of an Imploding Aluminum Liner Z-Pinch," Appl. Phys. Ltrs. Vol 31, 477, Air Force Weapons Laboratory, Kirtland AFB, NM,(1977).

19. Chase, L.F., Jordan, W.C., Perez, J.D., and Johnston, R.R., "X-Ray Spectrum of a Laser Produced Iron Plasma," and X-Ray Diagnostics for Laser Systems, LMSC-D401229, Lockheed, Palo Alto, California, (1974).

20. Dozier, D.M., et. al., "Sensitivity of X-Ray File II. Kodak No-Screen Film in the 1-100 KeV region," J. Appl. Phys. 47, 3732 (1976).

21. Benjamin, R. F., Lyons, P. B., and Day, R. H., "X-Ray Calibration of RAR 2490 Film for Application to Laser Plasma Experiments," LA-UR-76-1502 Los Alamos Scientific Laboratories, Los Alamos, New Mexico (1975).

22. Henke, B. L., and Tester, M.A., "Techniques of Low Energy X-Ray Spectroscopy," Adv. in X-Ray Analysis 18, 76 (1975), edited by W. L. Pickles, C.S. Barrett, and J. B. Newkirk, C. O. Rund, Plenum Press.

23. Fowler, C. M., Caird, R. S., and Garn, W. B., "An Introduction to Explosive Magnetic Flux Compression Generators," LA-5890-MS, Los Alamos Scientific Laboratories, Los Alamos, New Mexico, (1975).

DATE
FILMED

3-8